Contents lists available at ScienceDirect

International Journal of Heat and Fluid Flow

Numerical investigation of various twisted tapes enhancing a circular microchannel heat sink performance

Abdullah Masoud Ali [a,b], Aldo Rona [a,*], Matteo Angelino [a]

[a] *School of Engineering, University of Leicester, Leicester LE1 7RH, UK*
[b] *Faculty of Engineering, Sabratha University, P.O. Box 250, Sabratha, Libyan Arab Jamahiriya*

ARTICLE INFO

ABSTRACT

The continuous power increase and miniaturization of modern electronics require increasingly effective thermal management systems. The thermo-hydraulic performance of water-cooled L×L square-base silicon microchannel heat sinks is investigated by a conjugate heat transfer and computational fluid dynamics model over the Reynolds number range 100 to 500. Water at a constant inlet temperature of 298 K runs through 33 parallel tubes, extracting heat from the bottom wall that has a 100 W/cm^2 constant heat flux input. Hydro-thermal performance-enhancing tape inserts are numerically tested featuring (i) radial gaps between the tape and the tube, (ii) tape twist with axial pitch distances of ∞, L/2, or L/4, (iii) zero, one, or two 90-degree angular steps between consecutive tape segments, (iv) alternating clockwise and anti-clockwise consecutive twisted tape segments, and combinations of these features. The radial gaps produce both a hydraulic and a thermal performance loss. All combinations of tape twist, angular steps, and twist direction reversal produced better thermal performance gains to hydraulic loss trade-offs than the baseline microchannel configuration with no tape. The microchannel heat sinks with four L/4 alternating pitch consecutive helical tape segments provided the lowest bottom wall average temperature, 16.13 K below that with not tape, at the same Reynolds number of 500. This predicted temperature drop is a significant achievement towards conditioning electronic components so they may be longer-lasting, use less energy, and have a reduced environmental impact.

1. Introduction

Many micro-devices, such biomedical and micro-electronic circuits, chemical reactors, and micro-electro-mechanical systems, produce heat as they operate (Alfaryjat et al., 2019). Therefore, suitable cooling processes are essential to running these micro-devices. Dissipating the high heat flux through these devices is a technological challenge (Kandlikar and Bapat, 2007; Waqas et al., 2022). The research community is currently active in exploring means for improving the cooling performance of the heat sinks in these micro-devices. Kandlikar and Grande (Kandlikar and Grande, 2003) termed the heat sinks with channel hydraulic diameters ranging between 10 μm and 200 μm as microchannel heat sinks. Microchannel heat sinks can provide effective cooling in challenging, high heat flux dissipation problems from the electronics industry (Waqas et al., 2022; Deng et al., 2021).

An array of microchannel cooling passages can be carved into a matrix made from a thermally conducting material. How the matrix material choice affects the overall thermal performance was explored by testing heat sinks made in copper (Kleiner et al., 1995), aluminium (Choquette et al., 1996), bronze (Gamrat et al., 2005), silicon (Zhimin and Fah, 1997), stainless steel (Peng et al., 1994), and glass (Koşar, 2010). The matrix material choice was observed to be more significant in channels of larger height. Sub-millimetre lower high channels, for which the overall thermal performance is less sensitive to the matrix material choice, often use silicon as opposed to aluminium or copper. Silicon provides a lighter heat sink, which is desirable in light-weight electronic applications. The flow and heat transport through microchannel passages depends on the coolant type. The performance of various coolants has been studied, including that of water, methanol (Peng et al., 1994), other refrigerants (Zhuan and Wang, 2013), and of nanofluids (Mohammed et al., 2011; Ali et al., 2022). Gaseous coolants, including air (Kleiner et al., 1995), argon, helium, nitrogen (Harley et al., 1995), and ammonia (Adham et al., 2012), were also used. The

---

A. Masoud Ali et al.gation">A. Masoud Ali et al.   *International Journal of Heat and Fluid Flow 98 (2022) 109065*

Nomenclature

Symbols

A	Cross-sectional area, m^2
Cp	Constant pressure specific heat capacity, J/kg
D_h	Hydraulic diameter, m
f	Friction factor
h	Convection heat transfer coefficient, $W/(m^2.K)$
k	Thermal conductivity, W/(m.K)
L	Channel length, m
Nu	Nusselt number
Nu_x	Local Nusselt number
p	Pressure, Pa
P	twisted tape pitch
Pp	Pumping power, W
$\dot{q}$	Heat flux, W/m^2
R	Total thermal resistance, W/K
Re	Reynolds number
T	Temperature, K
u	Fluid velocity, m/s
V	volume flow rate, m^3/s

Greek symbol

Δp	Pressure drop, Pa
μ	Viscosity, kg/(m.s)
ρ	Density, kg/m^3

Subscripts

bf	base fluid
f	fluid
in	inlet
s	solid

---

most used coolants are water and air, owing to their low cost and wide availability. Liquid coolants are a useful alternative to gaseous coolants in applications where gaseous coolants are unable to meet the cooling demand.

The performance of microchannel heat sinks is documented at laminar and turbulent flow conditions. A few studies made use of both types of flow conditions (Tunc and Bayazitoglu, 2002). The studies that exploited laminar flow conditions feature more in the literature. Their popularity is due to the flow through the narrow bore channels being most often naturally laminar. The channels are also short, so that turbulence is unable to develop over the short channel length (Adham et al., 2013). Microchannel heat sinks have the potential to dissipate heat well (Jang and Choi, 2006), to provide a nearly uniform heated wall temperature distribution (Deng et al., 2021), they can be easy to implement (Bhandari and Prajapati, 2021), and can have a low power consumption. This potential is not achieved in typical microchannel heat sinks with a parallel and straight layout, which can feature high power consumption, a large temperature gradient, and poor heated wall temperature uniformity. Hence, the hydrothermal performance of conventional microchannel heat sinks must be improved. It is possible to achieve this by shape and structural optimisations of the microchannel, for instance, by using different microchannel cross-sectional shapes (Wang et al., 2016; Jing and He, 2019; Barba et al., 2006), groove and fins on the channel wall (Chai et al., 2018; Chai et al., 2019; Ali et al., 2021), a vortex generator (Awais and Bhuiyan, 2018; Lu and Zhai, 2019; Wu and Tao, 2008), or a biomimetic tree-like design (Jing et al., 2020; Mondal et al., 2014).

Wang, et al. (Wang et al., 2016) studied numerically the effect of the channel cross-section shape on the microchannel heat sink thermal performance. They modelled channel cross-sections in the shape of a rectangle, of a triangle, and of a trapezium. Their numerical predictions show that the rectangular cross-section provides the highest thermal performance, while the triangular cross-section provides the lowest one, among the three shapes. Ali, et al. (Ali et al., 2021) performed conjugate heat transfer simulations of microchannel heat sinks using discrete finite-volumes. They evaluated the effects of twisted and zigzag fin inserts into a plain rectangular microchannel. They determined that the twisted fin improved the cooling efficiency, whilst the zigzag fin delivered the best thermal performance. Wu and Tao (Wu and Tao, 2008) numerically examined the thermal characteristics of a rectangular microchannel that featured a longitudinal vortex generator. They reported that the longitudinal vortex generator was able to enhance the thermal performance of this type of heat sink. Chen and Cheng (Chen and Cheng, 2005) investigated microchannel heat sinks with biomimetic tree-like shapes. Their study identified tree-shaped channels able to boost the thermal performance, mainly due to a coolant perfusion effect

into the solid matrix that is provided by the channel tree-like network, which mimics blood perfusion in a biological tissue. Alternative approaches to changing the coolant path through a rectangular cross-section microchannel are making the path wavy (Mohammed et al., 2011) or tapering the channel (Hung and Yan, 2012). These changes improve the overall thermal performance or lower the heat sink thermal resistance. However, it was observed that these enhancements come at the cost of a higher pumping power.

Larger flow devices, such as industrial heat exchangers, have been modelled and tested with swirl flow generators inserted in their pipes. Swirl flow generators are passive devices that enhance flow mixing at a low pressure drop cost, to improve the heat transfer rate. Twisted tapes have been used as swirl generators in heat exchangers (Alam and Kim, 2018). As the coolant is driven past a twisted tape, the tape imparts a swirl motion to the coolant. This induced swirl velocity disturbs the thermal boundary layer over the coolant channel walls and promotes flow mixing. This results in a higher heat transfer coefficient than in a circular channel without any twisted tape (Ponnada et al., 2019). The interest by the research community in this concept is evidenced in the reviews on it from Deng, et al. (Deng et al., 2021); Webb, et al. (Webb and Kim, 2005); Manglik and Bergles (Manglik and Bergles, 2003), and Varun, et al. (Varun et al., 2016). Several variants to having a single, uninterrupted tape running through the full channel length have been explored, such interrupting the tape with axial gaps, adding tape pitch angle steps along its length, alternating between a clockwise and an anti-clockwise tape pitch along its length, varying the tape pitch, adding fringe cuts to the tape, using a twisted tape with centre wings on alternate axes, and using wire nails in the twisted tapes.

He, et al. (He et al., 2018) documented the effect of inserting a twisted tape on the friction factor and on the heat transfer of cross-flow air heaters. Their study confirmed that the flow swirl increases the heat transfer compared to a purely axial flow, at the cost of a higher pressure drop in the resulting turbulent flow. Eiamsa-Ard, et al. (Eiamsa-Ard et al., 2015) examined the trade-off between the heat transfer gain and the pressure loss from running between one and three twisted tapes in a corkscrew pattern through a pipe. Their experiment shows that one twisted tape filament in a corkscrew pattern gives the best heat transfer enhancement to pressure drop penalty trade-off. The use of multiple twisted tapes to improve the heat transfer in a pipe was studied experimentally by Eiamsa-ard (Eiamsa-ard, 2010); Bhuiya, et al. (Bhuiya et al., 2013), and Singh, et al. (Singh et al., 2016). Their research shows that the friction factor and the Nusselt number both increase as the number of twisted tapes increases.

Eiamsa-ard and Promvonge (Eiamsa-ard and Promvonge, 2010) considered configurations in which the tape twist axis coincides with the pipe axis. They explored the effect of tape pitch distance, of alternating

2

clockwise and anti-clockwise contiguous tape segments, and of adding tape pitch angle steps of 30, 60, and 90 degrees between contiguous segments. The 90 degrees step gave the best heat transfer enhancement. Abolarin, et al. (Abolarin et al., 2019) independently confirmed that the heat transfer increases by increasing the step angle, for the twist angle steps 0, 30, and 60 degrees. Ali, et al. (Ali et al., 2021) applied the continuous tape configuration (0 degrees twist angle step) with a pitch distance $P = L/2$, shown in Fig. 1 (c), to a silicon microchannel. They reported a 37 % lower thermal resistance compared to the microchannel without tape, at the cost of 66 % more pumping power.

To enhance the performance of pipe heat exchangers, Tusar, et al. (Tusar et al., 2019); Guo, et al. (Guo et al., 2011) and Khoshvaght-Aliabadi and Feizabadi (Khoshvaght-Aliabadi and Feizabadi, 2020) used twisted tapes with a gap between the tape and the pipe wall, while Bazdidi-Tehrani, et al. (Bazdidi-Tehrani et al., 2020) and Eiamsa-ard, et al. (Eiamsa-ard et al., 2010) also used tapes in contact with the pipe wall. Both configurations are reported to give a higher thermal performance at some pressure drop penalty compared to having no tape. However, no investigation has been found that provides a direct comparison between a twisted tape pipe insert with and without pipe wall clearance, in a microchannel heat sink. This investigation aims to address this knowledge gap first.

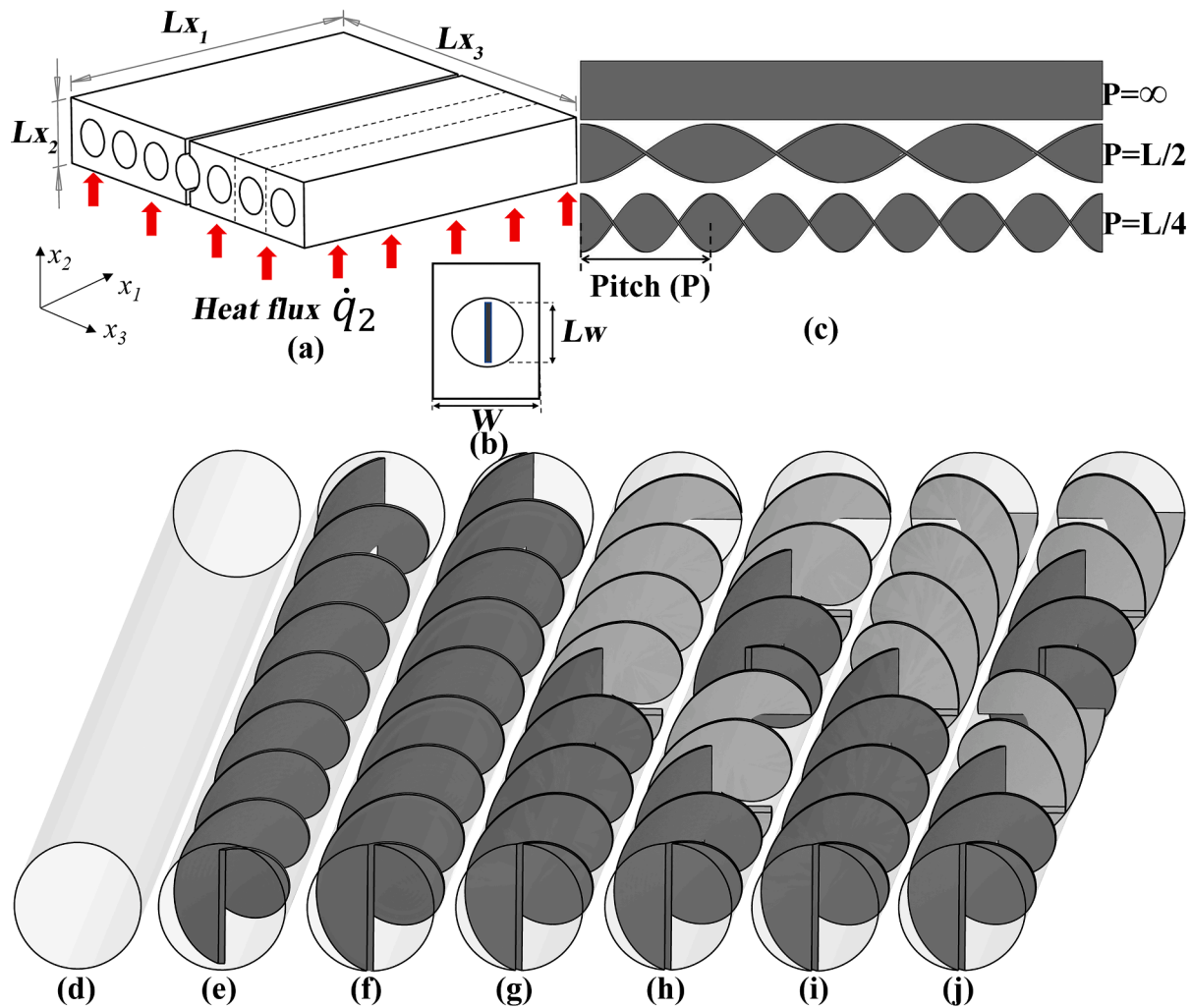Then, this investigation provides additional contributions to the field

by detailing the combined effects of pitch distance and twist direction reversal in the 90 degrees pitch step angle configuration Eiamsa-ard and Promvonge (Eiamsa-ard and Promvonge, 2010) found being the most conducive to heat transfer. Specifically, this research examines the effect of (i) inserting a single twisted tape in a circular microchannel heat sink with and without a gap between the tape and the channel wall, for the pitch distances $P = \infty$, $P = L/2$ and $P = L/4$, as shown in Fig. 1(e and f), and (ii) inserting head to tail two or four twisted tape segments of individual pitch distance $P = L/4$ with a tape pitch angle step of 90° as shown in Fig. 1(g-j).

These forced-convection microchannel heat sink configurations are modelled over the Reynolds number range $100 \le Re \le 500$, based on the channel hydraulic diameter and the 298 K coolant water entry temperature. The numerical predictions for the thermal and the hydraulic performance are referenced to the baseline configuration of the forced-convection microchannel heat sink with no tape (MC-NT) from Ali, et al. (Ali et al., 2021).

2. Methodology

2.1. Conjugate heat transfer approach

A three-dimensional control volume conjugate model is constructed

Fig. 1. (a) Isometric view of the circular microchannel heat sink wafer, (b) pitch distance, (c) front view of the microchannel, (d) no tape (MC-NT), (e) L/4 pitch single twisted tape with radial gaps (MC-TT-G-P = L/4), (f) L/4 pitch single twisted tape (MC-TT-P = L/4), (g) L/4 pitch two twisted tapes (MC-2TT-P = L/4), (h) L/4 pitch four twisted tapes (MC-4TT-P = L/4), (i) L/4 pitch two alternating twisted tapes (MC-2ATT-P = L/4), and (j) L/4 pitch four alternating twisted tapes (MC-4ATT-P = L/4).

with the aim of solving the velocity, the pressure, and the temperature fields of the heat sink, as Fig. 1(a) illustrates. To define the model, the following assumptions are made:

The flow is single-phase, laminar, steady, and incompressible.
The temperature-dependent thermal properties of fluid are steady.
The effect of gravity on the heat sink laid out horizontally as in Fig. 1 (a) is small.
The close to ambient temperature range generates negligible radiative heat transfer.

Using these assumptions, the flow governing equations reduce to the incompressible scalar transport equations in Cartesian orthogonal coordinates x_i (Cheng, 2007).

$$\frac{\partial \phi}{\partial t} + \frac{\partial}{\partial x_j}\left(\rho_f u_i \phi\right) = \frac{\partial}{\partial x_j}\left(\Gamma \frac{\partial \phi}{\partial x_j}\right) + S \tag{1}$$

where

$$\phi = \left(1, u_i, T_f\right)^T \tag{2}$$

$$\Gamma = \left(0, \mu_f, \mu_f/Pr_f\right)^T \tag{3}$$

$$S = \left[0, -\frac{\partial p_f}{\partial x_i}, 0\right]^T \tag{4}$$

where ρ_f, μ_f, Pr_f and u_i are the working fluid density, the molecular viscosity, the Prandtl number, and the velocity vector. p_f and T_f are the absolute pressure and the absolute temperature. Superscript T indicates the vector transpose.

$$Pr_f = \frac{\mu_f Cp_f}{k_f} \tag{5}$$

The temperature distribution across the microchannel heat sink walls is provided by the Laplace equation (Cheng, 2007):

$$\frac{\partial^2 T_s}{\partial x_j^2} = 0 \tag{6}$$

Equations (1) and (6) are solved under the following constraints at the microchannel exterior solid boundaries, microchannel openings, and at the fluid–solid interfaces:

Boundary conditions of the conjugate heat transfer simulation.

1.	Channel inlet	$u_1 = u_{in}, u_2 = u_3 = 0$	for fluid $T_f = T_{in} = 298$ K
			for solid $\frac{\partial T_s}{\partial x_1} = 0$
2.	Channel outlet	$p_f = p_{out} = 1$ atm	for fluid $\frac{\partial T_f}{\partial x_1} = 0$
			for solid $\frac{\partial T_s}{\partial x_1} = 0$
3.	The upper wall		$\frac{\partial T_s}{\partial x_2} = 0$
4.	Left and right walls	(symmetry)	solid $\frac{\partial T_s}{\partial x_3} = 0$
5.	Bottom wall		$-k_s \frac{\partial T_s}{\partial x_2} = \dot{q}_2 = 100$ W/cm^2
6.	Inner wall (fluid/solid surface)	$u_1 = u_2 = u_3 = 0$	$-k_s \frac{\partial T_s}{\partial x_n} = -k_f \frac{\partial T_f}{\partial x_n}$
7.	Tape walls (fluid/solid surface)	$u_1 = u_2 = u_3 = 0$	$-k_s \frac{\partial T_s}{\partial x_n} = -k_f \frac{\partial T_f}{\partial x_n}$

where n, k_f and k_s are, respectively, the coordinate normal to the wall and the thermal conductivities of the working fluid and of the solid wall.

2.2. Numerical solver

In the current work, the model of section 2.1 is implemented in the computational fluid dynamics software ANSYS FLUENT 19.5. The governing equations in the solid and fluid domains are discretized by the finite volume approach and integrated numerically by the SIMPLE scheme (Li et al., 2020). The approximate solutions to the mass, momentum, and energy governing equations are iterated by the standard pressure scheme and by second-order upwind discretisation (Li et al., 2020). When the normalised residual values are less than 1×10^{-8} for the energy equation and 1×10^{-6} for the other variables, the numerical solutions are deemed to have converged (Ghani et al., 2017). The temperature and the heat flux across the fluid–solid domain interfaces are obtained by solving the conjugate heat transport problem through the solid portion of the microchannel, by solving the heat conduction equation (the Laplace equation) (Ali et al., 2021). Radenac, et al. (Radenac et al., 2014) reports this method of coupling the Navier-Stokes and the heat conduction equations as highly robust, based on Giles' stability analysis. The computational cost of the typical simulation to convergence was found to be approximately 40 core hours on a 3.2 GHz shared memory high-performance computer cluster. The wall time was reduced by Message Passing Interface parallelization over 16 cores, using the METIS domain decomposition.

2.3. Geometry and boundary conditions

Fig. 1(a) shows the representation of a square-base heat sink with circular microchannels running through it, parallel to one another, in which the cooling water flows, evenly heated from below. In this case, 33 parallel circular tubes run through a silicon wafer of square base, along x_1. For clarity, seven out of the 33 tubes are diagrammatically shown in Fig. 1(a). The 33 tubes make up an array of tubes in x_3, out of which only one tube is modelled, to reduce the complexity of the simulation. The temperature field is imposed symmetric between adjacent tubes at the cross-sectional planes shown by the dashed lines in Fig. 1(a). Different tape inserts are modelled in the microchannel, as Fig. 1(d-j) illustrates. The microchannel with no tape (MC-NT) is modified by adding a tape with radial gaps along its long edges (MC-TT-G-P = L/4) or a tape with no gap (MC-TT-P = L/4), as shown in Fig. 1(d-f), respectively. Other arrangements in Fig. 1(g-j) show tape inserts having a pitch distance of P = L/4 and a 90 degrees pitch angle step between consecutive tape segments. These arrangements produce L/4 pitch two twisted tapes (MC-2TT-P = L/4) or L/4 pitch four twisted tapes (MC-4TT-P = L/4) or L/4 pitch two alternating twisted tapes (MC-2ATT-P = L/4), or L/4 pitch four alternating twisted tapes (MC-4ATT-P = L/4). Table 1 lists the main dimensions of the microchannel heat sink and of the tape.

As most modern integrated circuit chips are made by silicon, a microchannel heat sink created in silicon is also considered here. In theory, the heat sink block could be laminated on top of a microprocessor, the lamination process enabling the construction of the channels by stratification. The tape insert could be fabricated by heating and twisting a silicon plain sheet, then seating the tape by CO_2 laser welding (Ali et al., 2021). Alternatively, a heat sink in copper or other metals could be printed using either metal binder jetting or metal powder bed fusion, which are near-net shape manufacturing methods (Ali et al., 2021).

Table 2 lists the thermo-physical properties of the solid and fluid domains. The Reynolds number is between 100 and 500, the inlet

Table 1
Dimensions of the circular microchannel heat sink, in mm.

Lx_1	Lx_2	Lx_3	D_{h_N}	D_{h_G}	$D_{h_{NG}}$	W	Lw	Twisted tape thickness
10	0.4	10	0.2	0.181	0.18	0.3	0.18	0.01

Table 2
The thermo-physical properties of silicon (Wang et al., 2011), and water.

Material	ρ(kg m^{-3})	Cp(J/kg.K)	k(W/m.K)	μ(N·s/m^2)
Silicon	2330	710	148	–
Water	998.2	4182	0.6	0.001003

temperature T_{in} of the working fluid is fixed at 298 K, and the heat flux input is 100 W/cm^2. The Reynolds number at the inlet of the microchannel heat sink is defined as:

$$Re = \frac{\rho u_{in} D_h}{\mu} \qquad (7)$$

$$D_h = D - \frac{4A}{P} = D - \frac{4ab}{2(a+b)} = D - \frac{2ab}{a+b} \qquad (8)$$

In equation (8), A is the tape cross-section area, P its perimeter, and a and b are the width and thickness of the tape. If there is no tape, $D_h = D$.

2.4. Data reduction

The thermal performance of the circular microchannel heat sink with twisted tape is assessed via conventional heat transfer quantities. The convection heat transfer coefficient h of the microchannel heat sink and its average h_{avr} are (Bahiraei and Heshmatian, 2017):

$$h = \frac{k_f \left(\partial T_f / \partial x_n\right)}{T_{max} - T_m}$$

and

$$h_{avr} = \frac{\dot{q}_2}{T_{max} - T_m} \qquad (9)$$

In equation (9), T_{max} is the average bottom wall temperature and $\dot{q}_2$ is the heat flux vector normal to the bottom wall, into the wall, from an external heat source.

$$T_m = \frac{T_{in} + T_{out}}{2} \qquad (10)$$

In equation (10), T_{out} is the outlet temperature of the fluid leaving the microchannel heat sink.

The local Nusselt number Nu_x and the average Nusselt number Nu are defined as (Ghasemi et al., 2017):

$$Nu_x = \frac{D_h \left(\partial T_f / \partial x_n\right)}{T_{max} - T_m} \qquad (11)$$

and

$$Nu = \frac{h_{avr} D_h}{k_f} \qquad (12)$$

The total thermal resistance is defined as (Ghasemi et al., 2017):

$$R_{Total} = \frac{T_{max} - T_{in}}{\dot{q}_2} \qquad (13)$$

The friction factor f of each individual microchannel tube is given by (Ghasemi et al., 2017):

$$f = \frac{2 D_h \Delta p}{\rho_f u_{in}^2 L x_1} \qquad (14)$$

where

$$\Delta p = p_{in} - p_{out} \qquad (15)$$

is the pressure drop of the working fluid between the inlet and the outlet (Bahiraei et al., 2019). The pumping power supplied to the microchannel heat sink is given by (Bahiraei et al., 2019) as

$$P_p = V \Delta p \qquad (16)$$

where V is the volume flow rate.

The cooling performance of each microchannel design in Fig. 1 (d-j) is examined to assess whether adding swirl in the flow is beneficial or otherwise. A Figure of Merit (FoM) is used to calculate the overall thermo-hydraulic performance by comparing the change in the average Nusselt number to that in the friction factor (Bahiraei et al., 2019). This is evaluated as

$$FoM = \frac{Nu/Nu_0}{(f/f_0)^{1/3}} \qquad (17)$$

where subscript 0 denotes the microchannel configuration of Fig. 1(d), with no tape. The Figure of Merit aims to express, in a minichannel heat sink, the trade-off between any rate of heat extraction enhancement and the associated pumping power change that this entails. In this work, the Figure of Merit is used as a quantitative dashboard indicator to compare the performance of different heat sink configurations. Whereas the Figure of Merit is not an exhaustive quality indicator for microchannel heat sinks since, for instance, does not explicitly account for any heat sink contact temperature limits, its usefulness will be shown in producing a first ranking of different microchannel heat sink configurations in section 3.5.
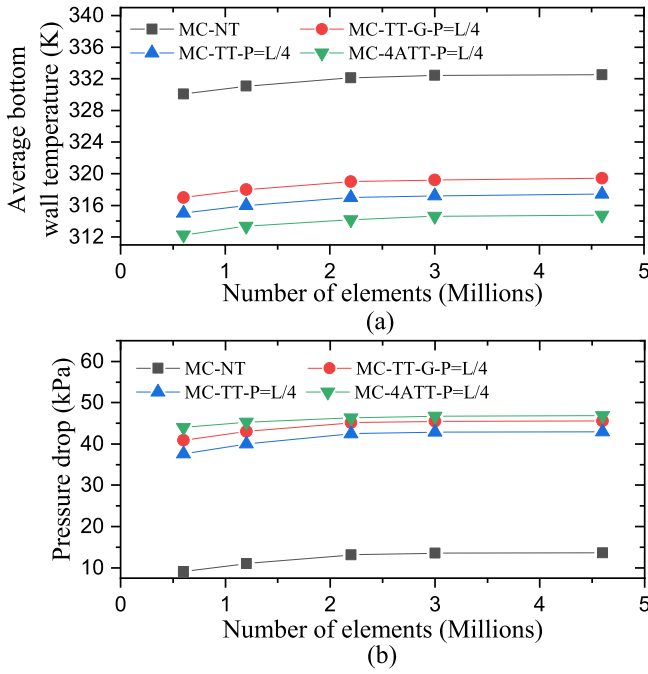
2.5. Grid independence

The sensitivity of the predictions to the spatial discretization of the computational domain is assessed based on the average bottom wall temperature and on the pressure drop across the microchannel. These parameters are selected as these are often key technical specifications in heat sink product sheets. In this study, a coarse mesh is progressively refined until these two parameters display an appreciable mesh independence. A hexahedral mesh is used because it provides greater accuracy and less simulation time than tetrahedral or mixed element meshes (Bahiraei et al., 2019). Accommodating the tape twist in a structured mesh topology required some alteration to the baseline mesh without any tape. Therefore, the mesh convergence assessment was performed both with and without a twisted tape, specifically for the configurations MC-NT, MC-TT-G-P = L/4, MC-TT-P = L/4, and MC-4TT-P = L/4 of Fig. 1, with water at Re = 300. Fig. 2 displays (a) the predicted average bottom wall temperature and (b) the pressure drop of the working fluid between the inlet and the outlet, against the number of elements. This figure displays no notable change either in the average bottom wall temperature or in the pressure drop as the number of elements is increased beyond 4.6 million. A more rigorous test of the spatial discretization dependence of the predictions is provided by determining the Grid Convergence Index (GCI), as defined by Roache (Roache, 1998). Let f_2 be the flow performance quantity of interest, in this case either the average bottom wall temperature or the pressure drop, predicted on a given computational mesh of N_2 elements, f_1 be the same performance quantity predicted on a finer mesh of $N_1 > N_2$ elements, and f_3 the one predicted on a coarser mesh. The mesh referment ratio $r_{1,2} = (N_1/N_2)^{(1/D)}$, where $D = 3$ is the number of independent spatial dimensions of the microchannel. For $r_{1,2} > 1.3$ (Roache, 1998), the order of the numerical scheme is empirically determined as

$$\widehat{P} = \frac{\left| \ln \left| \epsilon_{2,3} / \epsilon_{1,2} \right| + q(\widehat{P}) \right|}{\ln r_{1,2}} \qquad (18)$$

$$q(\widehat{P}) = \ln \left(\frac{r_{1,2}^{\widehat{P}} - s}{r_{2,3}^{\widehat{P}} - s} \right) \qquad (19)$$

$$s = \text{sign}\left(\epsilon_{2,3} / \epsilon_{1,2} \right) \qquad (20)$$

Fig. 2. Grid independence test results. (a) Microchannel average bottom wall temperature and (b) pressure drop across the microchannel.

Table 4

Grid convergence parameters based on the average bottom wall temperature of MC-NT.

Number of elements (million)	$\widehat{p}$	GCI	$\dfrac{GCI_{2,3}}{(r_{1,2}{}^{\widehat{P}}GCI_{1,2})}$
0.6			
		1.09	
2	1.92	2.52	1.061
4.6			

2.6. Model validation

The conjugate heat transfer model for the microchannel defined in sections 2.1 to 2.3 is validated by comparing its predictions against correlations for the friction loss and for the convective heat transfer in pipes, reported in the literature. The friction factors obtained from the model at different Reynolds numbers are compared against the corresponding Darcy friction factors for a fully developed laminar flow in a straight pipe with a circular cross-section, calculated from the Hagen-Poiseuille equation (Cengel, 2010). The Darcy friction factor is determined from $f = 64\,Re^{-1}$ (Cengel, 2010). This formula only applies to the hydrodynamically fully developed region. Therefore, the friction factor is evaluated from the static pressure change between the end of the entry length $L_h \cong 0.05Re D_h$ (Cengel, 2010) of the microchannel and the microchannel outflow, to exclude the hydrodynamic entrance region contributions to f. Fig. 4(a) shows that the friction factors from the numerical simulations agree well with the corresponding values from the Darcy law, as the two curves overlap. The substantial overlap between these two friction factor predictions in Fig. 4(a) provides confidence that the model can satisfactorily predict the microchannel hydraulic head loss over the Reynolds number range 100 to 500. Fig. 4(b) compares the predictions of the local Nusselt number for MC-NT from the conjugate heat transfer model to corresponding ones determined by the Shah correlation (Narendran et al., 2020) of equation (22). Fig. 4(b) displays, overall, a fairly good agreement between the two sets of predictions, with a maximum discrepancy of 5.7 %. More importantly, both methods differentiate well the non-dimensional heat transfer due to convection at different local Reynolds numbers, as expressed by the channel length on the abscissa, and exhibit the same monotonic trend. This enables the use of the microchannel conjugate heat transfer model with some confidence for the current comparative study of heat transfer in laminar pipe flow at different Reynolds numbers.

$$
Nu = \begin{cases} 1.953\left(RePr\dfrac{D_h}{x}\right)^{1/3} & \left(RePr\dfrac{D_h}{x}\right) \geqslant 33.3 \\ 4.364 + 0.0722\left(RePr\dfrac{D_h}{x}\right) & \left(RePr\dfrac{D_h}{x}\right) < 33.3 \end{cases} \tag{22}
$$

3. Results and discussion

In this section the thermal performance of the circular microchannel heat sink with several modified twisted tape designs is described.

3.1. Effects of twisted tape pitch on temperature distribution and flow pattern

Fig. 5 illustrates the temperature distributions on the bottom surface as well as on the inner wall of cases MC-NT, MC-ST, MC-TT-P = L/2, and MC-TT-P = L/4 at the Reynolds number of 500. The surface temperature distribution is presented in colour isolevels, with red indicating 335 K and blue 298 K. Fig. 5 shows that by introducing the straight tape (MC-ST), the bottom and the inner wall surface temperatures are reduced to below 308 K (in light blue) at the microchannel inlet and to approximately 327 K (in yellow) at the microchannel exit. Temperatures are further reduced to 304 K and 302 K at the inlet and to 319 K and 317 K at
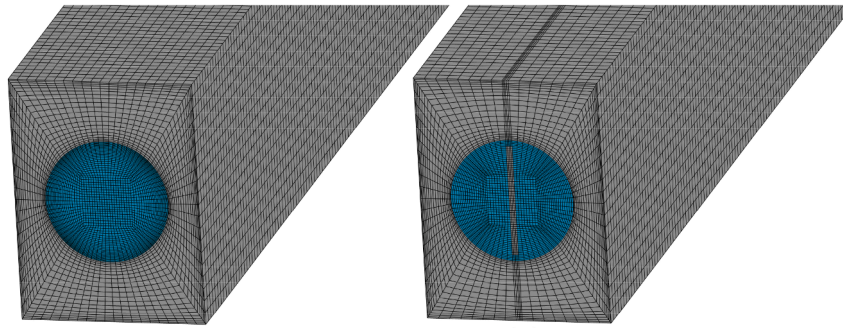
where the absolute error $\epsilon_{1,2} = f_2 - f_1$. Equation (19) is solved iteratively with the initial guess $q(\widehat{P}) = 0$ (Schwer, 2008).

The $GCI_{1,2}$ between two meshes N_1 and N_2 is determined as

$$
GCI_{1,2} = \frac{f_s|\varepsilon_{1,2}|}{\left(r_{1,2}{}^{\widehat{P}} - 1\right)} \tag{21}
$$

where the safety factor f_s is set to 1.25 when more than two grids are used (Roache, 1998). An appropriate spatial discretization provides predictions that fall in the asymptotic range of convergence, by which $GCI_{2,3}/\left(r_{1,2}{}^{\widehat{P}}GCI_{1,2}\right) \rightarrow 1$. Table 3 shows this parameter for the same configurations as in Fig. 2, based on the average bottom wall temperature (left column) and on the microchannel pressure drop (right column). Table 4 shows the mesh sizes used to compute this parameter for MC-NT, for reference. Table 3 indicates that the predictions obtained with the 2 million mesh as the N_2 mesh in equations (18) and (21) fall within the finite volume scheme asymptotic range of convergence by satisfying to a good approximation $GCI_{2,3}/\left(r_{1,2}{}^{\widehat{P}}GCI_{1,2}\right) = 1$.

Combining the CGI analysis and the observations from Fig. 2, the most refined mesh size of 4.6 million cells is selected for modelling all the cases. Fig. 3 shows the mesh topology for two of these cases.

Table 3

Ratio between observed spatial discretization errors over the expected ratio at asymptotic convergence $GCI_{1,2}/(r_{1,2}{}^{\widehat{P}}GCI_{2,3})$ based on the microchannel average bottom wall temperature and the pressure drop across the microchannel.

Microchannel configuration	Ratio based on the average bottom wall temperature	Ratio based on the pressure drop across the microchannel
MC-NT	1.061	1.056
MC-TT-G-P = L/4	1.065	1.041
MC-TT-P = L/4	1.054	1.033
MC-4ATT-P = L/4	1.048	1.032

Fig. 3. Three-dimensional computational mesh structure of MC-NT and of MC-ST-G.
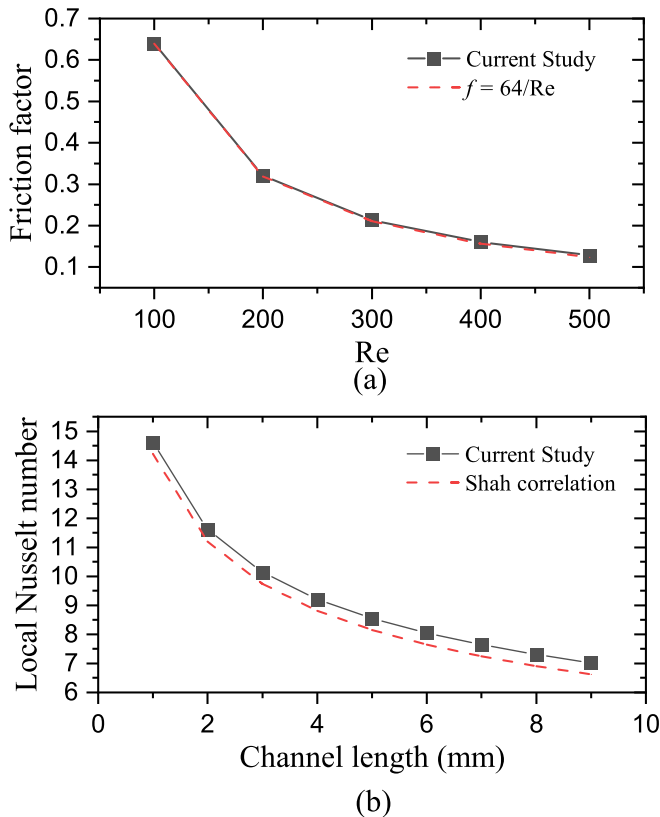

Fig. 4. Comparison of flow and heat transport predictions from the microchannel model to published correlations. (a) Friction factor and (b) local Nusselt number of MC-NT.

the exit, by twisting the tape with pitch distance L/2 (MC-TT-P = L/2) and L/4 (MC-TT-P = L/4), respectively.

Fig. 6 displays the temperature distribution in the cross-sectional plane through the middle of the microchannel heat sink with no tape and with a tape of pitch distance $P = \infty$, $P = L/2$, and $P = L/4$, at Re = 500. The maximum bottom wall temperature is obtained with the microchannel with no tape, whereas the minimum bottom wall temperature is obtained in the case with the pitch distance $P = L/4$. The tape acts as a heat bridge across the pipe, improving the heat transfer performance by increasing the internal wet surface area. A minor contribution is also thought to be produced by the axial conduction of heat along the tape from the outlet to the inlet due to the axial increase in temperature towards the outlet. Twisting the tape further reduces the thermal resistance between the solid and the fluid regions by generating a secondary swirl flow that increases the velocity of the fluid near the channel wall, as Fig. 7 and Fig. 8 illustrate.

To clarify the effect of the tape on the flow pattern in the microchannel heat sink, streamline distributions are presented in Fig. 7. The cases shown are MC-NT, MC-ST, MC-TT-P = L/2, and MC-TT-P = L/4 at Re = 500. The streamlines are coloured by flow velocity magnitude, with red corresponding to 5 m/s and blue to 0 m/s. Inserting the straight tape ($P = \infty$) raises the flow blockage because of the growing boundary layers on the tape surfaces, resulting in a slightly higher axial velocity away from the walls compared to the case with no tape. This effect, together with the increase of the internal wet surface area, contributes to the enhancement of the cooling performance at the expense of an increased flow resistance, and therefore of an increased pumping power. The twisted tape is shown in Fig. 7 to generate a swirl flow that increases the cooling performance but also the flow resistance, compared to the cases with no tape (MC-NT) and with a straight tape (MC-ST). A higher flow resistance is also obtained by decreasing the pitch distance from L/2 to L/4. Varying the Reynolds number over the range $100 \leq Re \leq 500$ results in a corresponding change in velocity and in similar swirl streamline patterns that are not shown here, for brevity. The Re = 500 condition provides the highest cooling performance due to its higher bulk velocity.

Fig. 8 displays the velocity magnitude distributions on the cross-sectional plane in the middle of the microchannel heat sink, with no tape and with a continuous tape of pitch distance $P = \infty$, $P = L/2$, and $P = L/4$, at Re = 500. The velocity magnitude is shown by colour isolevels, with red corresponding to 5 m/s and blue to 0 m/s, while the black vectors represent the in-plane velocity component. As it can be seen from these colour isolevels, the velocity magnitude of the microchannel without any tape (MC-NT) is highest at the centre and decreases towards the wall, as in a classical Hagen-Poiseuille type flow through a pipe. In the case with the inserted straight tape (MC-ST), the flow is divided into two equal parts, each part acting as a Hagen-Poiseuille type flow. Thus, case MC-ST shows an increased peak velocity compared to case MC-NT. Inserting a twisted tape with a pitch distance of L/2 increases the flow blockage and generates significant in-plane motion, or secondary flow, as shown in Fig. 8 by the black vectors. A stronger secondary flow is obtained by decreasing the pitch distance from L/2 to L/4. This swirl flow increases the heat convection in the transverse direction as it helps transport heated fluid away from the cooler microchannel top, which has an adiabatic wall, towards the hotter microchannel bottom, which has the heated wall. Varying the Reynolds number over the range 100 to 500 results in a corresponding change in velocity distribution and in-plane velocity vectors magnitude that is not shown here, for brevity. The flow pattern is consistent over this Reynolds number range. At Re = 500, the strongest swirl flow and therefore the highest cooling performance is predicted.

3.2. Effects of twisted tape radial gap and segmentation on temperature distribution and flow

Fig. 9 shows the temperature distributions on the bottom surface as well as on the inner wall for cases MC-TT-G-P = L/4, MC-TT-P = L/4,
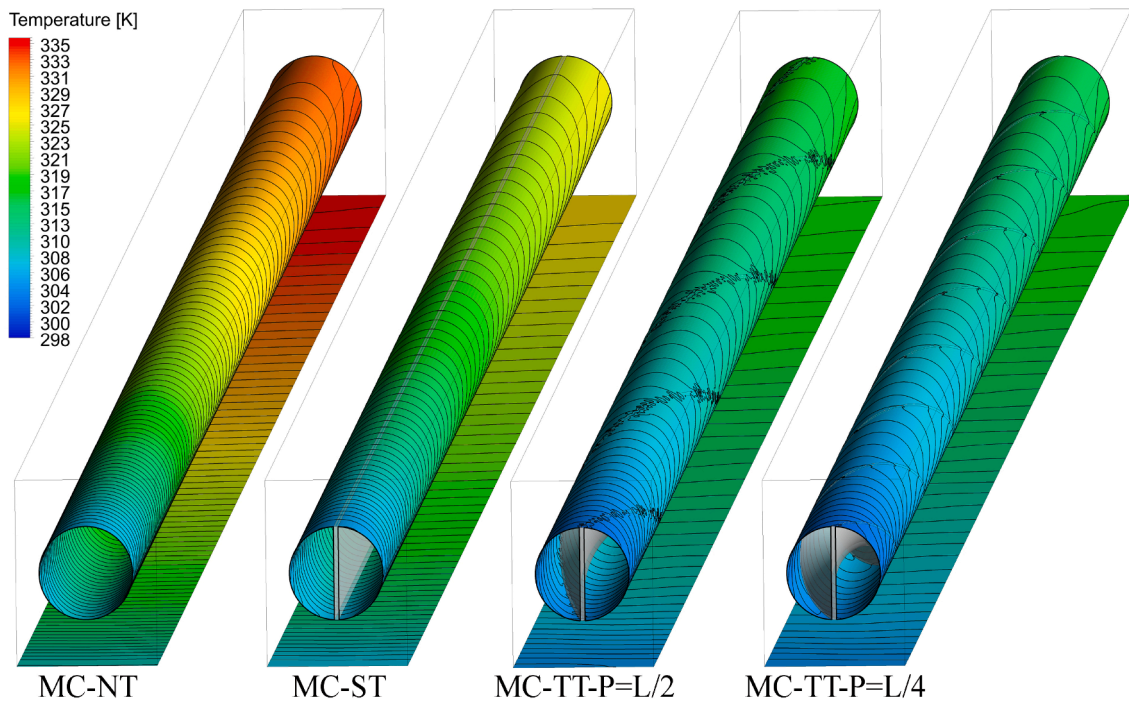
Fig. 5. Temperature colour isolevels on the bottom surface as well as on the inner wall of MC-NT, MC-ST, MC-TT-P = L/2, and MC-TT-P = L/4 at Re = 500.
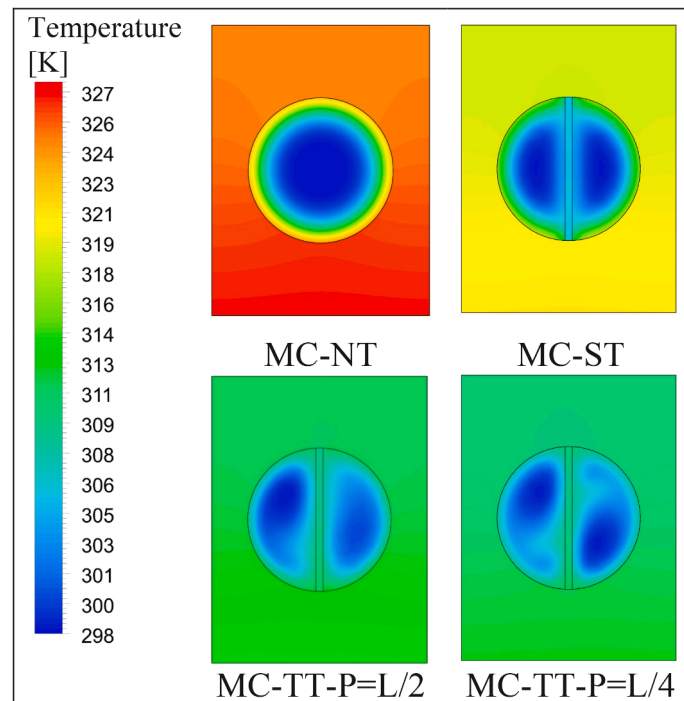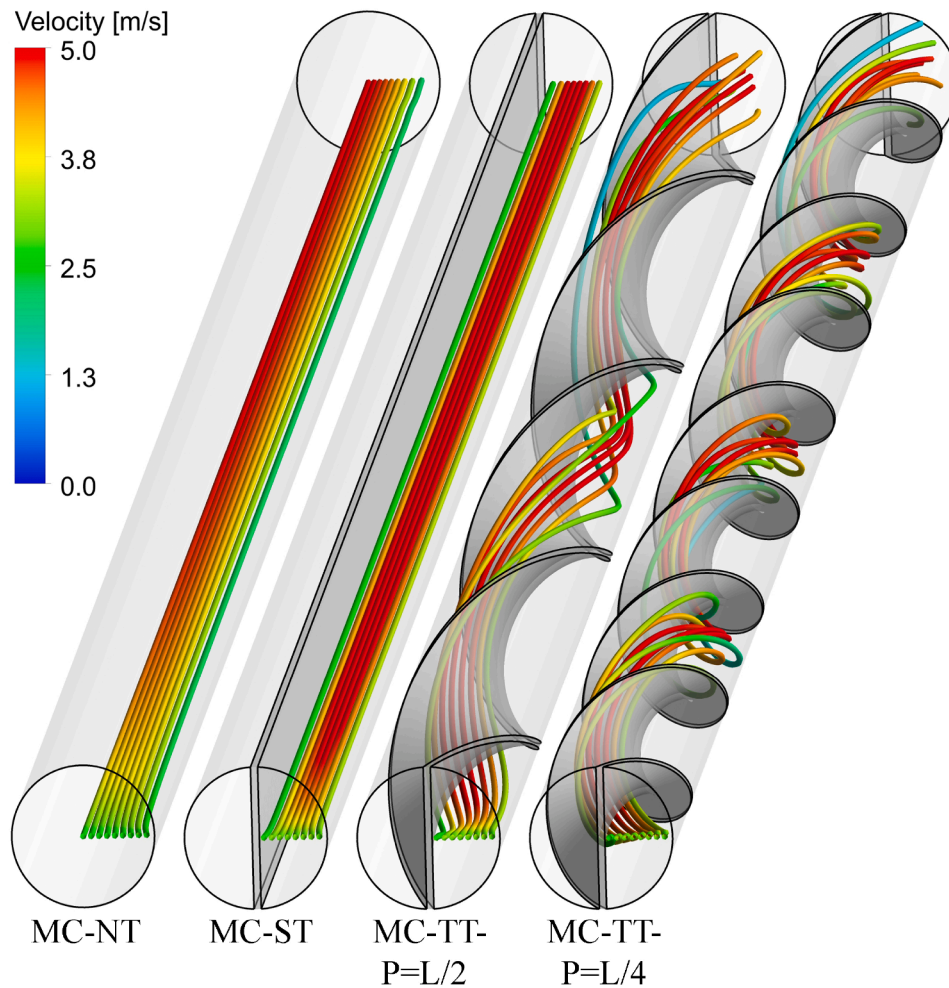

Fig. 6. Temperature distribution in the cross-sectional plane through the middle of the microchannel heat sink with no tape and with a tape of different pitch distances, at Re = 500.

MC-4TT-P = L/4, and MC-4ATT-P = L/4, at Re = 500. The surface temperature distribution is presented by colour isolevels, with red corresponding to 318 K and blue to 298 K. The temperature distribution in the microchannel without any radial gap (MC-TT-P = L/4) is lower than in the microchannel with radial gaps (MC-TT-G-P = L/4), indicating a lower thermal resistance, as illustrated in the discussion of Fig. 10. A further decrease in the average bottom wall temperature is achieved by splitting the twisted tape into L/4 pitch four twisted tapes (MC-4TT-P =

L/4), with an even further reduction obtained with L/4 pitch four alternating twisted tapes (MC-4ATT-P = L/4). The reason for this temperature reduction will be discussed in the context of Fig. 14 and Fig. 15. The effect of the number of tapes, not visualized here for brevity, indicates that L/4 pitch four twisted tapes (4TT and 4ATT) provide a better cooling performance compared to L/4 pitch two twisted tapes (2TT and 2ATT), respectively. The effect of the Reynolds number from 100 to 500 was also examined, showing that the surface temperature decreases by

Fig. 7. Streamlines in the microchannel heat sinks MC-NT, MC-ST, MC-TT-P = L/2, and MC-TT-P = L/4, at Re = 500. The streamlines are colour-coded by the velocity magnitude.

increasing the Reynolds number and that the lowest surface temperature is achieved at Re = 500.
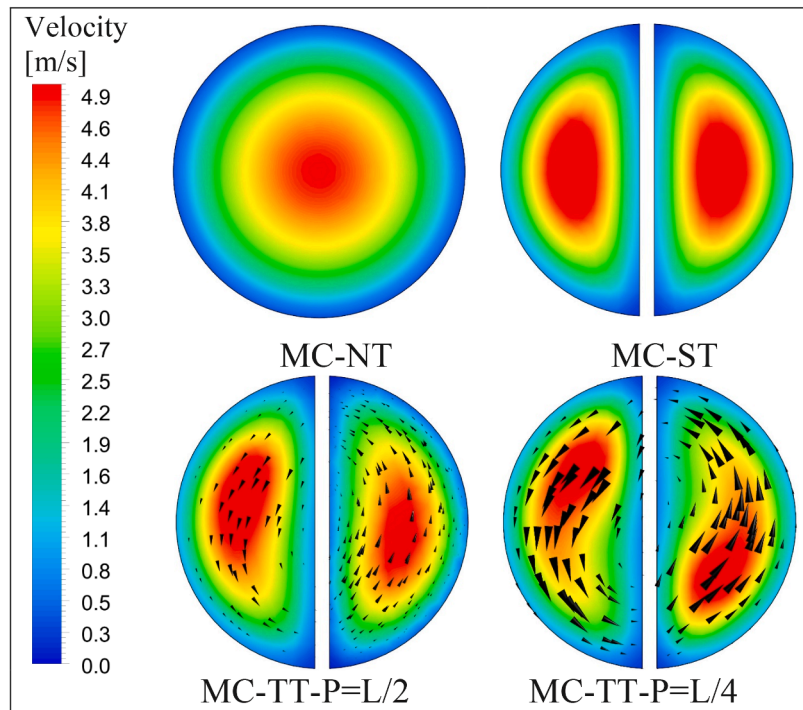
Fig. 10 shows the temperature distribution on the cross-sectional plane in the middle of the microchannel heat sink with different twisted tape designs, at Re = 500. The negative effect of the radial gaps along the tape top and bottom edges is clearly shown by the MC-G tape being colder. These gaps prevent the conduction of heat between the tape and the channel wall, which enhances the cooling performance of the microchannel in the case with no radial gap, as previously argued in the context of Fig. 6. As a result, the average temperature in the case MC-TT-P = L/4 is lower than in the case MC-TT-G-P = L/4. Cases MC-4TT-P = L/4 and MC-4ATT-P = L/4 show decreased temperatures and a more homogeneous temperature distribution. The L/4 pitch four alternating twisted tapes (MC-4ATT-P = L/4) produce the lowest thermal resistance among all the modelled configurations.

An analysis of the flow pattern is performed to explain these effects. Fig. 11 displays a radial rake of streamlines in the microchannel heat sink with the twisted tape designs MC-TT-G-P = L/4, MC-TT-P = L/4, MC-4TT-P = L/4, and MC-4ATT-P = L/4, at Re = 500. The streamlines are coloured by the flow velocity magnitude, with red corresponding to 5 m/s and blue to 0 m/s. The microchannel with radial gaps and the microchannel without gap MC-TT-P = L/4 appear to have the same twisting streamline pattern. The segmentation of the tape into four clockwise helices in MC-4TT-P = L/4 produces a stronger mixing but also a higher flow blockage. The L/4 pitch four alternating twisted tapes in MC-4ATT-P = L/4 produce a further increase in the flow blockage,
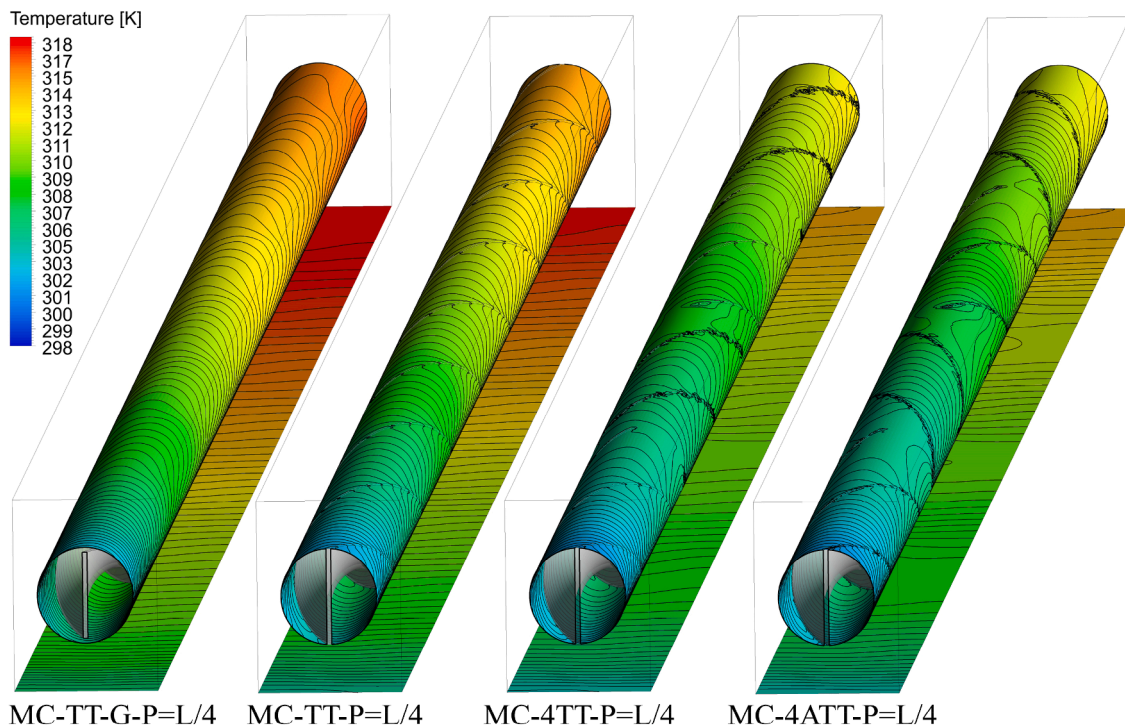
due to the change in the direction of the swirl shown by the streamlines, but lead to a more even mixing, as clarified in Fig. 14 and Fig. 15.

Fig. 12 shows the velocity magnitude distributions on the cross-sectional plane at $x_1 = 7$ mm from the inlet with the twisted tape designs MC-TT-G-P = L/4, MC-TT-P = L/4, MC-4TT-P = L/4, and MC-4ATT-P = L/4, at Re = 500. The microchannel with radial gaps along the tape perimeter MC-TT-G-P = L/4 is predicted to feature a slightly higher peak velocity magnitude than the microchannel without any gap MC-TT-P = L/4. This appears to be due to the additional flow resistance encountered by the flow in the vicinity of the gaps, where secondary flow features narrow the effective cross-section area. An even higher peak velocity magnitude and in-plane motion are obtained by segmenting the tape, by which the flow blockage is increased. Although Fig. 12 shows a somewhat higher peak velocity magnitude from the microchannel with the L/4 pitch four alternating twisted tapes MC-4ATT-P = L/4 compared to the microchannel with L/4 pitch four twisted tapes MC-4TT-P = L/4, additional flow changes are likely to underpin the heat performance difference between these two configurations.

The local Nusselt number distribution over the microchannel surfaces wetted by the coolant provides an insight into over which areas the transfer for heat from the microchannel walls to the coolant is most intense. The predictions in Fig. 13 display spirals of low local Nusselt numbers over the surface of the pipe, where the tape long edge of each spiral tape segment rests on the cylindrical surface. In the no-gap configurations, the three right-most channels in Fig. 13, the tape locally prevents the coolant from wetting the cylindrical surface and reduces

Fig. 8. Colour isolevels of velocity magnitude in the $x_1 = 5$ mm plane and in-plane velocity vectors at Re = 500. MC-NT, MC-ST, MC-TT-P = L/2, and MC-TT-P = L/4, viewed from the inlet.

Fig. 9. Temperature colour isolevels on the bottom surface and on the inner wall of MC-TT-G-P = L/4, MC-TT-P = L/4, MC-4TT-P = L/4, and MC-4ATT-P = L/4, at Re = 500.

the local flux of heat removal. Configuration MC-TT-G-P = L/4 displays the same low local Nusselt number spiral signature over the surface of the pipe, notwithstanding the gap this microchannel has between the tape and the pipe surface. The gap through-flow hydrodynamic resistance causes an effect similar to that from having no gap, by obstructing the local convection cooling by water. Still, the water that manages to

flow through the gap provides some heat extraction, as indicated by the higher local Nusselt number achieved in MC-TT-G-P = L/4 along the spiral footprint compared to the other three configurations shown to the right of it.

Adding 90 degrees pitch angle steps along the tape, as in configurations MC-4TT-P = L/4 and MC-4ATT-P = L/4, is shown in Fig. 13(a)
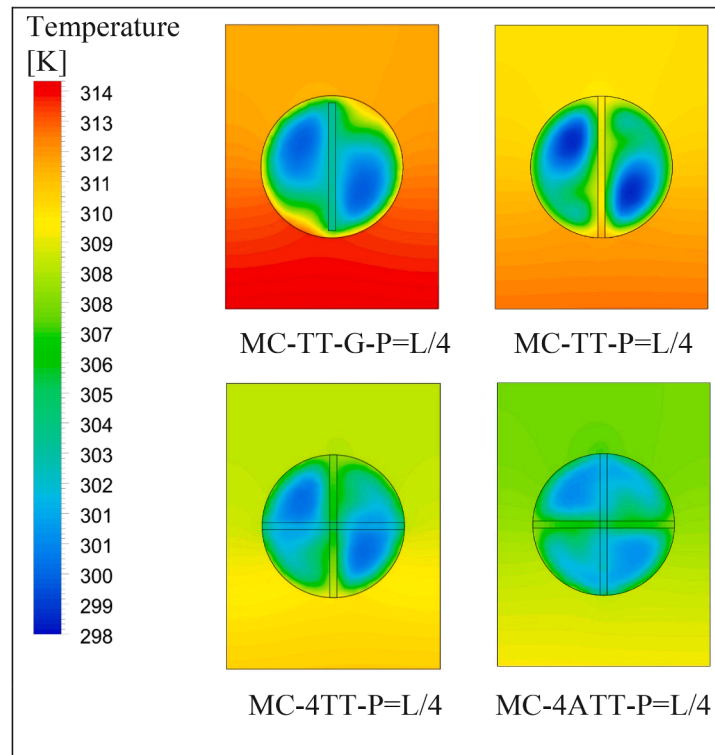
Fig. 10. Temperature distribution in the cross-sectional plane $x_1 = L/2$ with different twisted tape designs at Re = 500 and at a constant twist pitch distance P = L/4.

and (b) to introduce a new feature in the distribution of local Nusselt number over the surface of the pipe. Areas of enhanced local Nusselt number, shown by lighter shading in Fig. 13(a) corresponding to approximately $Nu_x = 14$, appear in the first spiral half-turn that follows downstream the pitch angle step. The extent and shape of these areas differ between having tape segments twisted in the same direction, in MC-4TT-P = L/4, and having alternating clockwise and anti-clockwise tape segments, in MC-4ATT-P = L/4. In MC-4TT-P = L/4, the area is more localised to the first spiral half-turn that follows the pitch angle step, in MC-4ATT-P = L/4, the area extends over almost one full turn of the tape spiral. Fig. 13(b) displays the local Nusselt number distribution over the bottom half of the pipe surface, which is the portion of the cylindrical surface that lies closest to the microchannel heated floor. The local Nusselt number distribution follows approximately the same pattern as that over the top half of the pipe surface of Fig. 13(a), but the greater proximity to the heated floor causes higher temperature gradients, leading to higher local Nusselt number values. These higher values of the local Nusselt number are denoted by the lighter shading indicating $Nu_x = 20$ in the first spiral half-turn downstream of the pitch angle step.

Fig. 12 and Fig. 13 have shown differences of in-plane velocity and of local Nusselt number from alternating the pitch direction. To further investigate these differences, Fig. 14 shows selected streamlines for cases MC-4TT-P = L/4 and MC-4ATT-P = L/4 at Re = 500. The streamlines are generated from an annular source at the inlet with a diameter of around 0.16 mm at a distance from the inlet of 2.45 mm. As it can be seen from these streamlines, using four helical tape segments with alternating directions in MC-4ATT-P = L/4 tends to radially push the streamlines from the axis of the microchannel towards the near-wall region more than by using only clockwise twisted tape segments in MC-4TT-P = L/4. This behaviour reduces the thermal resistance by offering further convection heat transfer along the microchannel inner cylindrical wall and produces a more homogeneous temperature distribution in comparison to the case MC-4TT-P = L/4, as shown in Fig. 10.

This effect on the streamlines can be explained by analysing the flow behaviour around the leading edge of each new helix. The Q-criterion, as introduced by Hunt, et al. (Hunt et al., 1988), identifies a vortical

structure where $Q = 1/2(\|\Omega\| - \|S\|) \rangle 0$, i.e. where the norm of the vorticity tensor Ω dominates that of the strain rate tensor S. Fig. 15 shows isosurfaces of Q, coloured by the velocity component u_2 normal to the leading edge, with red corresponding to 2 m/s and blue to –3 m/s, thus indicating the direction of rotation of the vortices. Where the helix has the same direction as the preceding one, the streamlines are aligned with the new helix as they approach its leading edge. Vortical structures are mainly due to the presence of a blunt leading edge and are therefore relatively symmetric on the two sides of the tape about the channel axis, as indicated by the label 1 in Fig. 15. With helices of alternating directions, however, the streamlines approach the leading edge of the new helix at non-zero incidence, due to the change in the direction of the tape twist. This produces a stronger flow separation on one side of the tape, with rotational symmetry, as indicated by the label 2 in Fig. 15, and a more attached flow on the opposite side. The overall result is a stronger mixing and therefore an enhanced thermal performance, as discussed in the following section.

3.3. Effects of twisted tape design on thermal characteristics

The convective heat transfer relative advantage of microchannel heat sinks with tape over the no tape configuration of Fig. 1(d) is shown in Fig. 16, where the average Nusselt number ratio (Nu/Nu_0) from the configurations of Fig. 1(e-j) are reported over the Reynolds number range 100 to 500. Subscript 0 refers to the microchannel without any tape. For reference, Table 5 lists the Nusselt number, the pressure drop, and the friction factor predicted from the microchannel heat sink model without any tape. It is noted that the average Nusselt number ratio monotonically increases with increasing Reynolds number, so that the tape inserts are predicted to facilitate heat convection more at the higher Reynolds numbers. Fig. 16 shows that the average Nusselt number ratio of the microchannel without any radial gap, of Fig. 1(f), is higher than that from the microchannel with radial gaps, of Fig. 1(e), at any given Reynolds number. This advantage is attributed to the heat conduction between the tape and the heat sink cylindrical inner wall, as these surfaces touch one another in Fig. 1(f). The absence of any tape radial gap
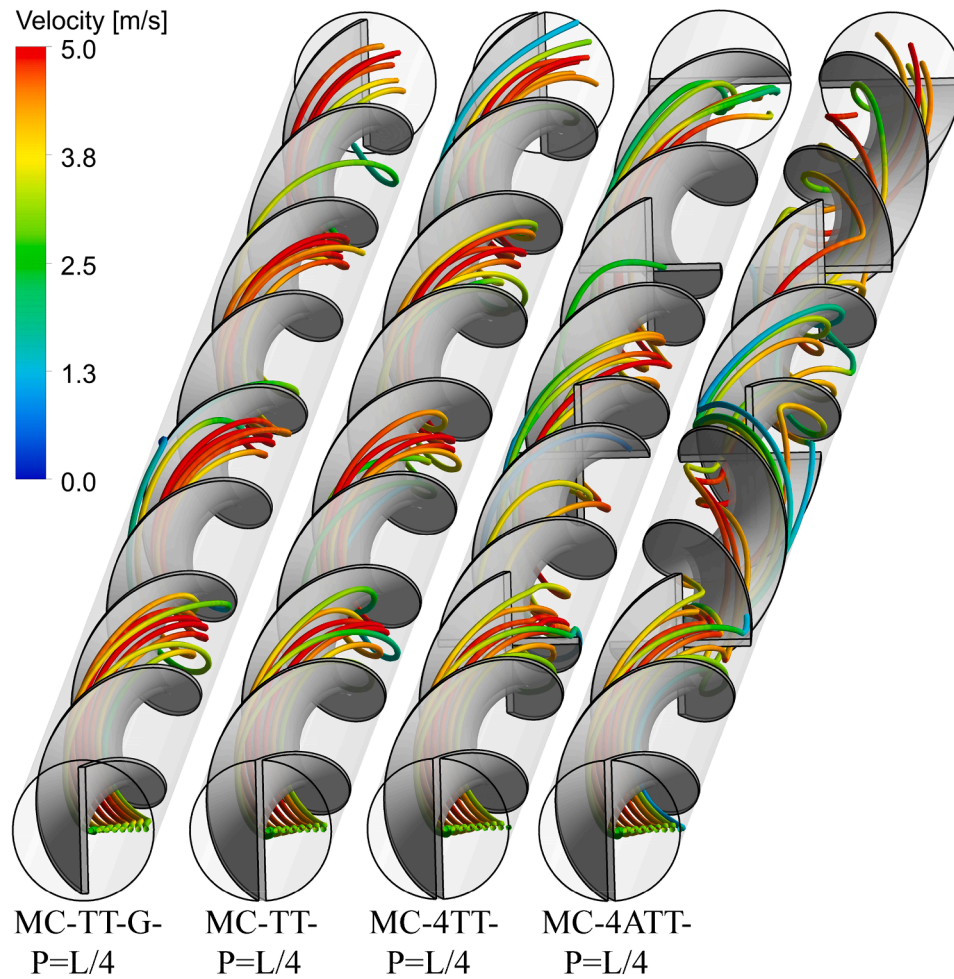
Fig. 11. Streamlines through the microchannel heat sinks MC-TT-G-P = L/4, MC-TT-P = L/4, MC-4TT-P = L/4, and MC-4ATT-P = L/4, at Re = 500. The streamlines are colour coded by the velocity magnitude.

also marginally increases the tape heat transfer surface area. Fig. 16 shows that inserting a straight tape already provides about a 20 % higher average Nusselt number, depending on the Reynolds number, compared to not having any tape. Twisting the tape increases this advantage. Reducing the twisted tape pitch distance from L/2 to L/4, i.e. using a tape helix finer pitch, provides a further gain in the predicted average Nusselt number ratio. With this finer pitch, coolant flow parcels, guided by the tape, follow a longer path from the microchannel inlet to the microchannel exit, so they get an extended exposure to the heated microchannel walls. This provides more distance over which to extract heat from the microchannel inner surface.
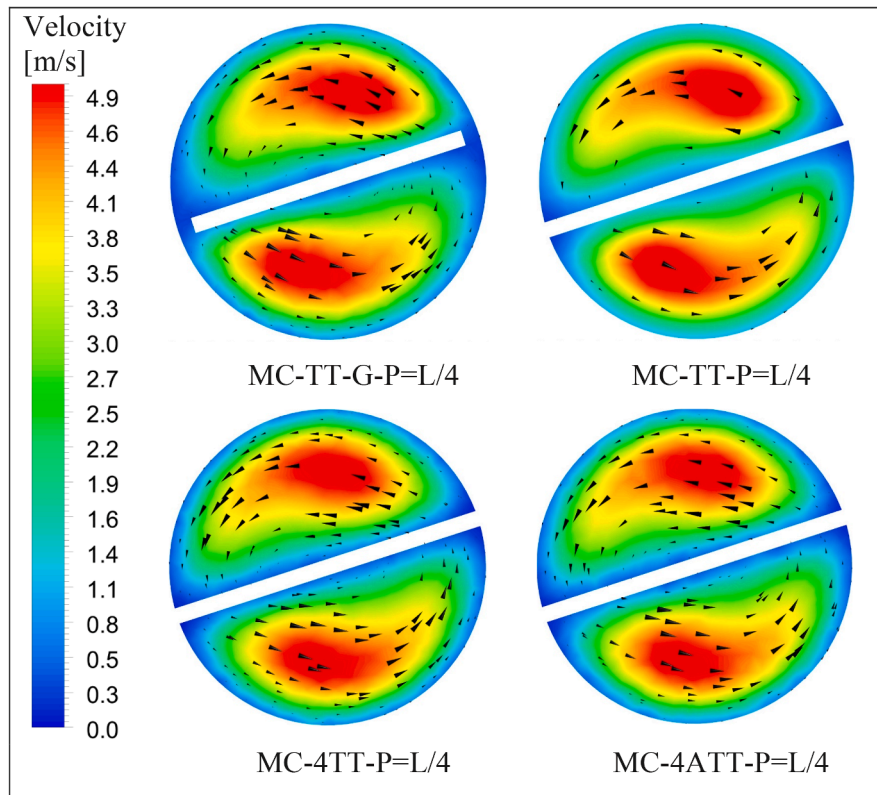
Fig. 16 shows that the technique by Eiamsa-ard and Promvonge (Eiamsa-ard and Promvonge, 2010) and by Abolarin, et al. (Abolarin et al., 2019) of inserting a 90 degrees tape pitch angle step, by segmenting the tape, works well in the silicon microchannel heat sink configuration of Fig. 1. Using the tape made up of two silicon segments twisted in the same direction (MC-2TT-P = L/4) of Fig. 1(g) confers a higher average Nusselt number ratio than having a single tape helix throughout the microchannel length. Increasing the tape segmentation from two to four (MC-4TT-P = L/4), as in Fig. 1(h), increases this gain. The flow study presented in section 3.2 advances the state of the art by providing evidence to explain the performance gain from the pitch angle steps in a microchannel heat sink. This gain is probably due to the generation of a fresh, thin thermal boundary layer at the leading edge of each new tape segment. The trailing edge of the preceding tape segment sheds a shear layer that promotes coolant flow mixing. Furthermore, the new helix appears to circulate the coolant towards the microchannel

bottom, which is closer to the heat source, over a shorter axial distance compared to an uninterrupted tape helix. These three effects combine to provide the observed heat transfer performance advantage.

Fig. 16 corroborates another interesting aspect from the work of Eiamsa-ard and Promvonge (Eiamsa-ard and Promvonge, 2010), which is the generation of a convective heat transfer advantage by alternating the direction of twist in consecutive tape segments. With microchannels as in Fig. 1(i) and (j), the average Nusselt number ratio labelled MC-2ATT-P = L/4 and MC-4ATT-P = L/4 is higher than the corresponding values labelled MC-2TT-P = L/4 and MC-4TT-P = L/4, which use only clockwise twist. The flow study in section 3.2 provides new, state of the art, important insight into the mechanism behind this gain, such knowledge being fundamental to exploiting this phenomenon in industrial products. By alternating the direction of the twist, the incoming flow produces a phenomenon akin to a leading-edge stall on the tape segment that follows. The stall reportedly diverts the coolant away from the tape surface, moving away from the centre of the microchannel towards the heated cylindrical walls. In this process, less hot coolant running through the channel centre replaces the warmer coolant running closer to the cylindrical walls. This provides a more uniform coolant through-flow temperature, as shown in Fig. 10. The average Nusselt number ratio gain is highest at Reynolds number 500, with a gain of 168.1 %, 155.33 %, 106.31 % and 76.13 % with respect to the MC-NT configuration for cases MC-4ATT-P = L/4, MC-4TT-P = L/4, MC-TT-P = L/4 and MC-TT-G-P = L/4, respectively.

Fig. 17 shows how the tape inserts of Fig. 1(e-j) affect the difference between the average temperature (T_{max}) of the heated bottom wall and

Fig. 12. Colour isolevels of velocity magnitude and in-plane velocity vectors 7 mm from the inlet of the microchannel heat sink, for different twisted tape designs, at Re = 500.

the temperature (T_{in}) of the coolant at the microchannel inlet, over the Reynolds number range 100 to 500. $T_{max} - T_{in}$ decreases monotonically with increasing Reynolds number in all the configurations of Fig. 1(d-j) irrespective of the presence of any tape. The largest temperature difference $T_{max} - T_{in}$ at all Reynolds numbers is obtained in the absence of any tape (MC-NT), as in Fig. 1(d). This difference is up to 57 K at the lowest Reynolds number of 100 and it represents a significant unwanted temperature overheat in the thermal conditioning of microprocessors and of microelectronic devices. Inserting a straight tape as in Fig. 1(e) lowers this temperature difference (MC-ST-G). Twisting the tape (MC-TT-G-P = L/2) and reducing the tape pitch (MC-TT-G-P = L/4) progressively reduces $T_{max} - T_{in}$.

Closing the radial gaps between the tape and the heated cylindrical wall, as in Fig. 1(f), provides a lower temperature difference in MC-ST than in the corresponding configuration with radial gaps of Fig. 1(e), MC-ST-G. Closing the radial gaps is likewise advantageous with twisted tapes of L/2 pitch, MC-TT-G-P = L/2 vs MC-TT-P = L/2, and of finer pitch L/4, MC-TT-G-P = L/4 vs MC-TT-P = L/4. This trend is displayed across the full Reynolds number range 100 to 500.

$T_{max} - T_{in}$ in MC-TT-P = L/4 is further reduced by inserting 90 degrees tape pitch angle steps, and two steps (MC-2TT-P = L/4) give a lower temperature difference than one step (MC-4TT-P = L/4). Alternating the direction of the tape twist (MC-2ATT-P = L/4 and MC-4ATT-P = L/4) provide a small incremental decrease in the temperature difference compared to using just clockwise twisted tape segments (MC-2TT-P = L/4 and MC-4TT-P = L/4). The T_{max} of MC-4ATT-P = L/4, MC-4TT-P = L/4, MC-TT-P = L/4 and MC-TT-G-P = L/4 are 16.13 °C 15.91 °C, 13.7 °C and 12.42 °C lower than the T_{max} with the MC-NT configuration at the Reynolds number of 500.
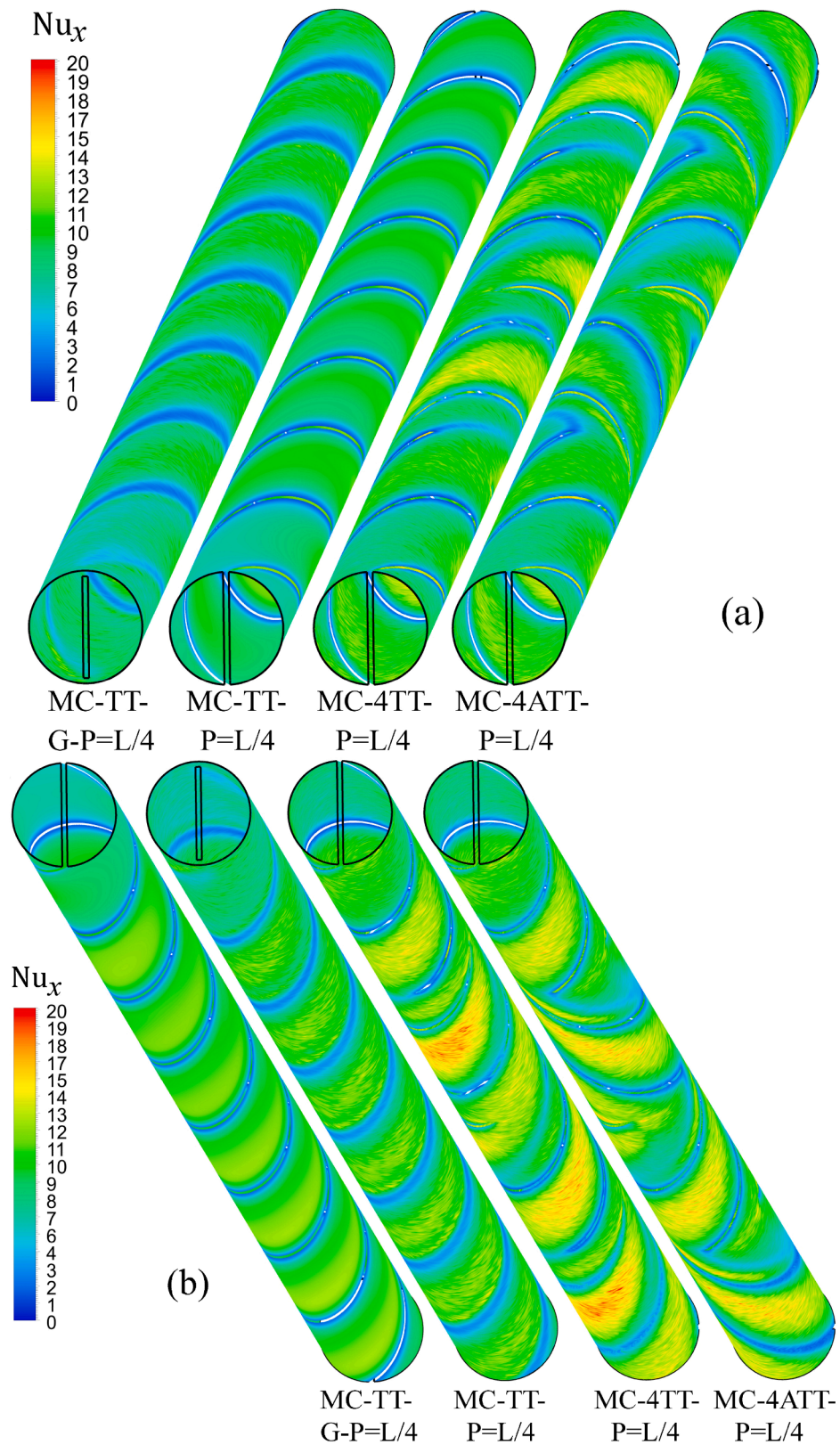
3.4. Effects of twisted tape design on hydraulic characteristics

Inserting a tape in a microchannel causes unwanted additional resistance to flow and Fig. 18 quantifies this effect in terms of the ratio between the pressure drop predicted with a tape to the one without a tape, $\Delta p/\Delta p_0$, over the Reynolds number range 100 to 500. All microchannel configurations with a tape insert are shown to have about three times the pressure drop of the microchannel without any tape MC-NT. The pressure drop of the microchannel without any tape increases monotonically with the Reynolds number, as shown in Table 5. Whereas $\Delta p/\Delta p_0$ predictions for configurations MC-ST-G, MC-ST, MC-TT-G-P = L/2, MC-TT-P = L/2, and partially MC-TT-P = L/4 have downwards trends with increasing Reynolds number, the raise of Δp_0 with Re in Table 5 produces a net rise in Δp with increasing Reynolds numbers, for all the modelled microchannel configurations. The pressure drop across all the microchannels with radial gaps is higher than that of the corresponding microchannel configuration without any radial gap, due to flow leakage through the gap creating secondary flows and a locally high shear stress past the gap. This pressure drop mechanism is akin to the blade tip leakage effect in unshrouded turbine blades, which experience larger passage losses than equivalent shrouded blades. Twisting the tape (MC-TT-P = L/2) increases the pressure loss compared to using a straight tape (MC-ST), more so if the pitch of the tape twist is finer (MC-TT-P = L/4).

Modifying the twisted tape MC-TT-P = L/4 by inserting 90 degrees tape pitch angle steps generates additional pressure drop in MC-2TT-P = L/4, which increases with the number of pitch angle steps in MC-4TT-P = L/4, and by alternating the direction of the tape helix (MC-2ATT-P = L/4 and MC-4ATT-P = L/4) in consecutive tape segments. At the Reynolds number of 500, the pressure drop (Δp) of MC-4ATT-P = L/4, MC-4TT-P = L/4, MC-TT-P = L/4 and MC-TT-G-P = L/4 are 269.5 %, 256.6 %, 220.99 % and 253.57 % higher than that from the MC-NT configuration, which is the microchannel without any tape.

The same increased flow resistance effect in microchannels with a tape in Fig. 18 can be expressed in terms of changes in the friction factor ratio f/f_0, as shown in Fig. 19. f/f_0 is the ratio of the friction factor

Fig. 13. Local Nusselt number for MC-TT-G-P = L/4, MC-TT-P = L/4, MC-4TT-P = L/4, and MC-4ATT-P = L/4, at the Reynolds number of 500. Distribution over the microchannel pipe internal surface, (a) top view, (b) bottom view.

predicted in a microchannel with a tape to the one predicted in the configuration MC-NT of Fig. 1(d), without any tape. Fig. 18 and Fig. 19 are identical but for a scaling factor on the ordinate. The friction factor, which is calculated using the Darcy equation, Eq. (14), is a function of the pressure drop, the hydraulic diameter, and the length of the microchannel. Since the microchannel length L is constant for all the microchannel configurations of Fig. 1(d-j), then $f/f_0 = (\Delta p/\Delta p_0)\left(D_h/D_{h_N}\right)^3$, at any given Reynolds number. The reduction in
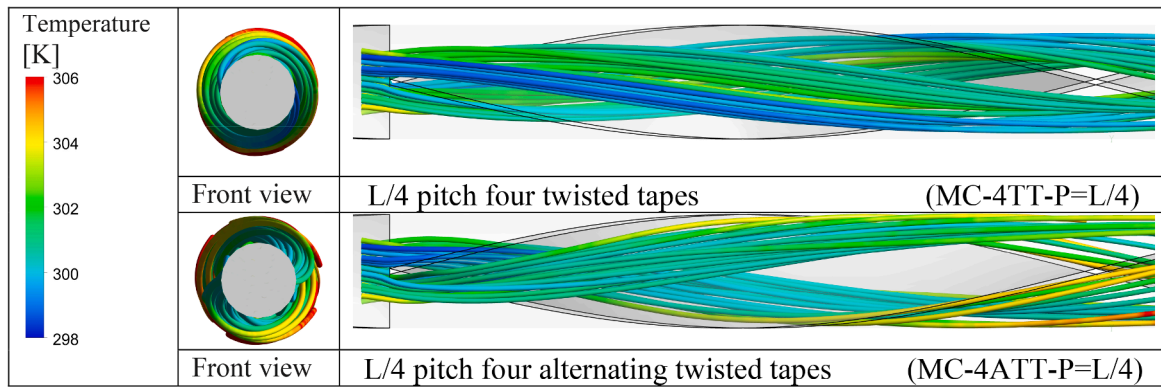
Fig. 14. Streamlines through microchannels with only clockwise twisted tape inserts MC-4TT-P = L/4 and with alternating clockwise and anti-clockwise twisted tape inserts MC-4ATT-P = L/4, at Re = 500. The streamlines are colour-coded by the temperature of the fluid.
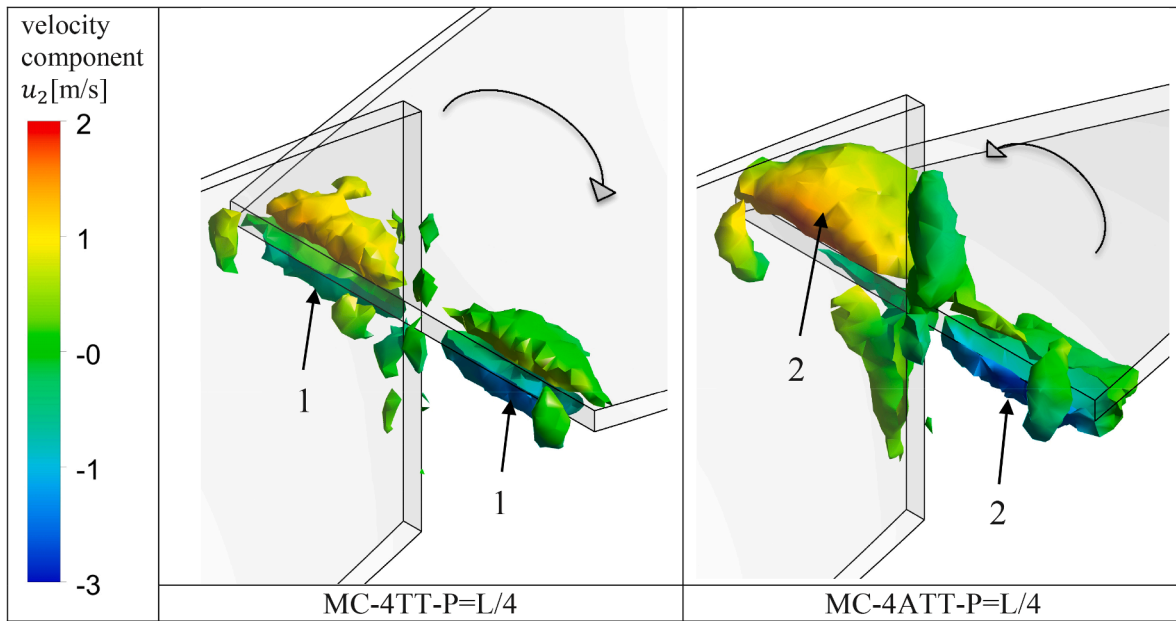

Fig. 15. Vortical flow structures for cases MC-4TT-P = L/4 and MC-4ATT-P = L/4, at Re = 350.

hydraulic diameter from inserting the tape reported in Table 1 generates the ordinate scaling factor between Fig. 18 and Fig. 19. MC-NT has the lowest friction factor, due to its lowest wetted wall surface area and its mainly axial through flow. The same observation was reported by Bazdidi-Tehrani, et al. (Bazdidi-Tehrani et al., 2020) in a tube. The friction factors (f) of MC-4ATT-P = L/4, MC-4TT-P = L/4, MC-TT-P = L/4 and MC-TT-G-P = L/4 are 173.66 %, 164.11 %, 137.73 % and 162.30 % higher than f_0 of the MC-NT configuration at the Reynolds number of 500.

3.5. Thermo-hydraulic performance trade-off of all microchannel configurations and ranking by the Figure of Merit.

The Figure of Merit (FoM) in Fig. 20 shows the trade-off between the gains in thermal performance, expressed by Nu/Nu_0, and the hydraulic losses incurred, expressed by f/f_0, as a tape insert is added to a cylindrical microchannel. The performance of the cylindrical microchannel with no tape (MC-NT) is used as a reference at each Reynolds number. Fig. 20 shows that the FoM from all the microchannel configurations with a twisted tape is above 1.0 and hence it is higher than that of MC-NT. Using a straight tape provides an unwanted, adverse trade-off of less than 1.0 at all Reynolds numbers, which is mainly due to a relatively

modest thermal performance gain against a more significant hydraulic loss penalty, for the configurations MC-ST-G and MC-ST. The trade-off is more adverse at the higher Reynolds numbers. Radial gaps between the tape edges and the cylindrical inner wall, in MC-ST-G, MC-TT-G-P = L/2, and MC-TT-G-P = L/4 lower the FoM compared to the corresponding configurations MC-ST, MC-TT-P = L/2, and MC-TT-P = L/4 without any radial gap. This is due to a combination of lack of thermal conduction between the tape and the cylindrical walls and of hydraulic loss caused by the tape gap through-flow, as inferred from Fig. 16 and Fig. 18, respectively. The FoM bars in Fig. 19 show that introducing one 90 degrees tape pitch angle step in MC-TT-P = L/4 provides an appreciable gain in the FoM (MC-2TT-P = L/4). Adding a second 90 degrees pitch angle step (MC-4TT-P = L/4) gives a further benefit in the FoM. Conversely, alternating the azimuthal direction of the tape twist in consecutive tape segments, like in MC-2ATT-P = L/4 and in MC-4ATT-P = L/4, provides a comparatively lower gain in the FoM over inserting tape segments of only clockwise twist, as in MC-2TT-P = L/4 and MC-4TT-P = L/4. Alternating the tape twist may therefore not provide an attractive uplift to the FoM over other configuration variants. The microchannel with fine pitch twist tape segments of alternating direction (MC-4ATT-P = L/4) provides the highest FoM among all the configurations tested in this study.
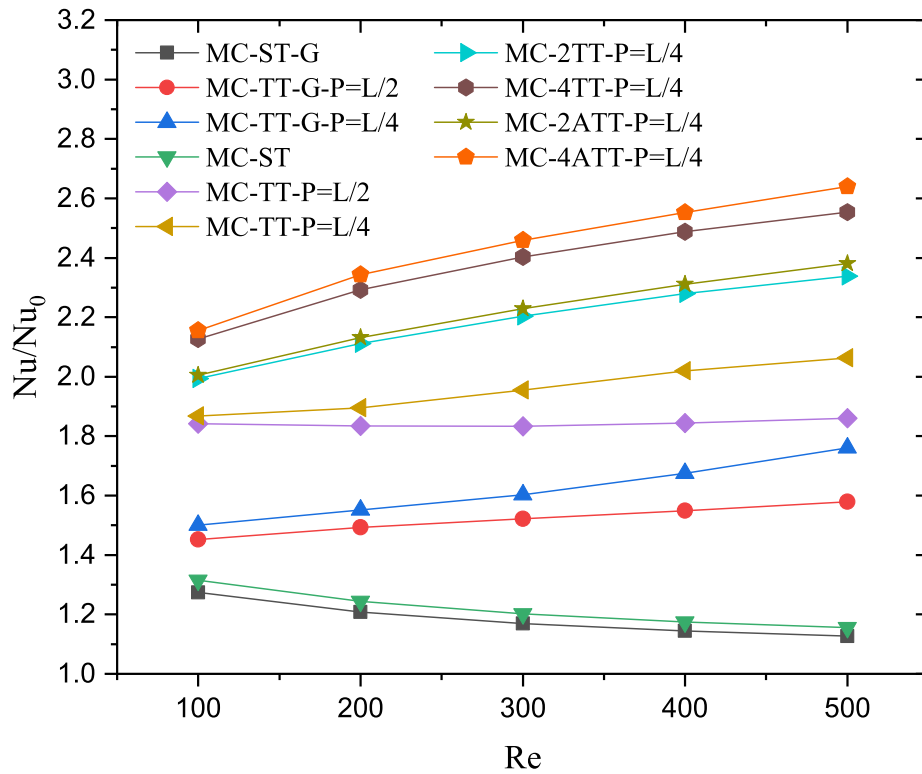
Fig. 16. Average Nusselt number ratio for all the microchannel configurations of Fig. 1, over the Reynolds number range 100 to 500.

Table 5
Average Nusselt number, pressure drop and friction factor of the microchannel heat sink without any tape MC-NT.

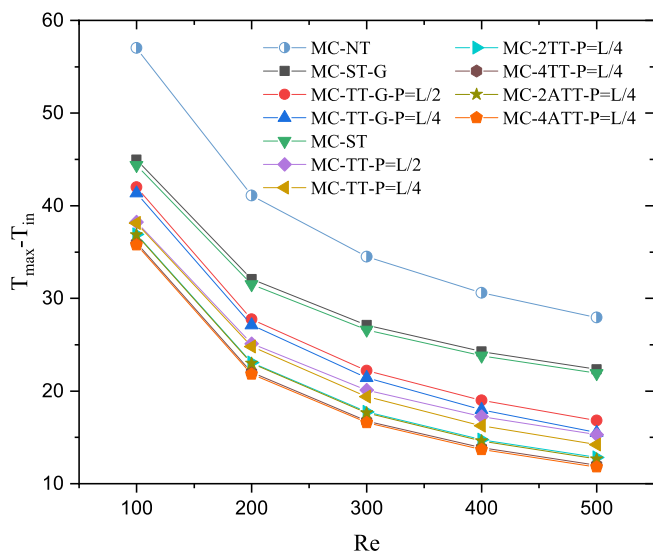| Re	100	200	300	400	500
Nu_0	11.17	13.07	14.45	15.59	16.57
ΔP_0 (kPa)	4.21	8.75	13.6	18.76	24.23
f_0	0.67	0.35	0.24	0.18	0.15

Fig. 17. Difference between the average bottom wall temperature (T_{max}) and the inlet flow temperature (T_{in}) in microchannels with different tape inserts, over the Reynolds number range 100 to 500.
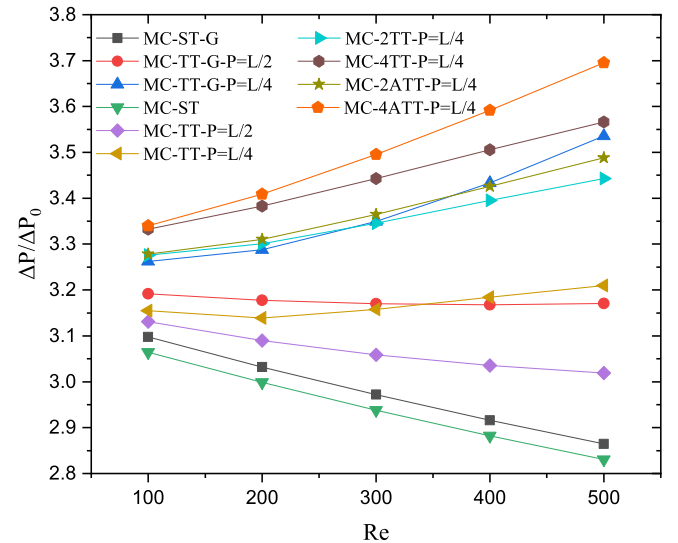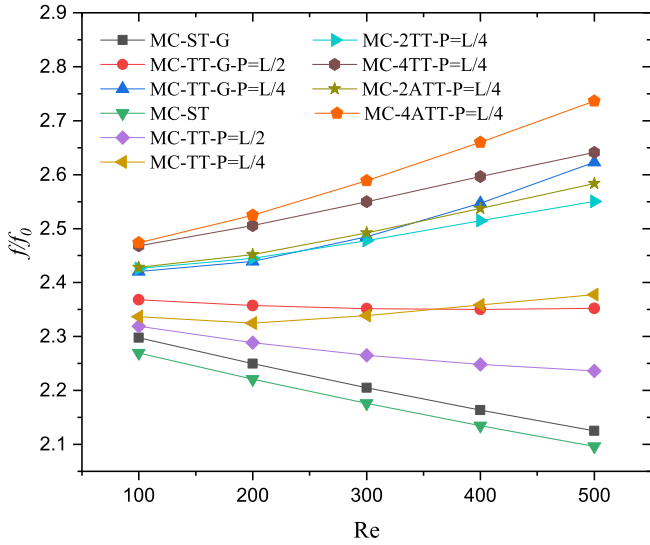

Fig. 18. Pressure drop across microchannels with various tape inserts normalised by the pressure drop across the microchannel without any tape MC-NT. Numerical predictions over the Reynolds number range 100 to 500.

Other studies proposed different insert designs for circular microchannels and the FoM is used to compare their performance with the ones in this study. Zheng, et al. (Zheng et al., 2021) evaluated a cone-column insert. Fig. 20 shows the FoM of the cone-column insert, referenced to the circular microchannel without insert in Zheng, et al. (Zheng et al., 2021). The FoM of this insert appears to peak at Re = 300, at which the FoM is just higher than that of MC-4ATT-P = L/4. The cone-column insert therefore would appear best exploitable with a quasi-constant coolant circulator pump, to match the Re = 300 heat sink regime. Liu, et al. (Liu et al., 2018) tested numerically an insert made by two tapes twisted about the microchannel axis that intersect one another

Fig. 19. Friction factor through microchannels with various tape inserts normalised by the friction factor from the microchannel without any tape MC-NT. Numerical predictions over the Reynolds number range 100 to 500.

at right angles, forming an equiaxial cross on all axial planes. This insert at the twist ratio of two is shown in Fig. 20 to deliver the highest FoM at Re = 400 and it would also best suit a quasi-constant coolant circulator pump, to match a Re = 400 heat sink regime. Whereas (MC-2TT-P = L/4) and (MC-2ATT-P = L/4) have a lower FoM than the inserts by Zheng, et al. (Zheng et al., 2021) and by Liu, et al. (Liu et al., 2018) at their respective optimal Reynolds numbers, their FoM increase monotonically with Reynolds number and may appeal to higher Reynolds number applications that use a variable circulator pump. It is possible that the feature responsible for this difference in behaviour is the 90 degrees tape pitch angle steps in MC-2ATT-P = L/4. The coolant radial push generated by these steps, discussed in the context of Fig. 14, may increase with increasing Reynolds number and, with it, the cooling of the microchannel circular walls that is provided by this secondary flow.
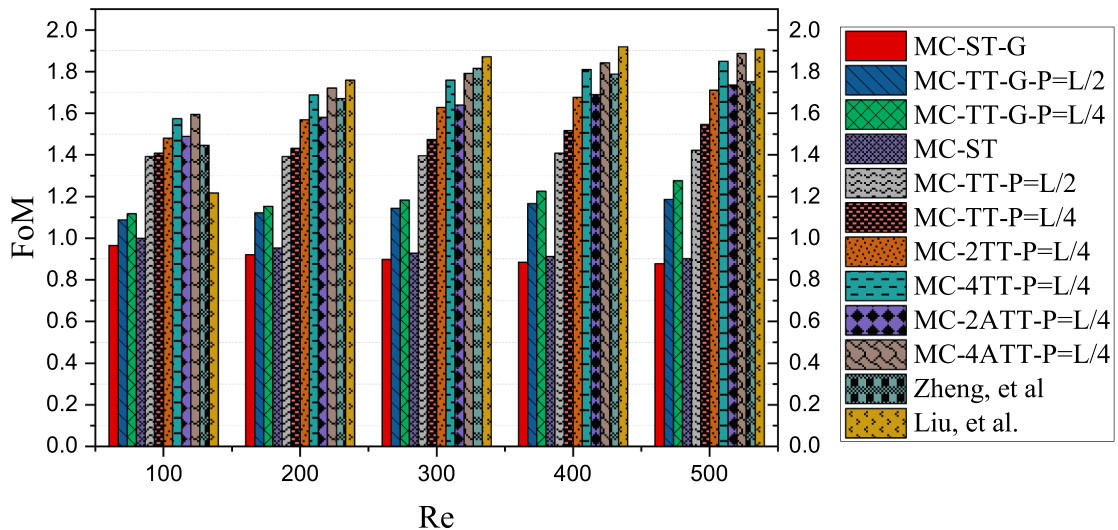
The microchannel in Fig. 1 with the highest Figure of Merit is the shape of highest geometric complexity among the tested configurations and, therefore, requires considerations on its manufacturing. Such considerations provide the groundwork for complementing the current numerical study with laboratory tests, to confirm the performance advantage identified in this work. Furthermore, these considerations can

be used to explore the path to the industrial production of such a design, as they expose some of the manufacturing challenges. Two alternative fabrication methods are considered, both of which involve inserting and securing twisted tape segments inside the baseline microchannel with no tape. To manufacture the baseline microchannel with no tape, a 10 mm square silicon wafer 0.4 mm thick can in principles be either cast or extruded complete with the 33 0.3 mm diameter through holes, or it can be cut from a larger slab and then the through-holes can be micro-drilled. The twisted tape segments can either be extruded through a die directly with the desired helical pitch or a straight tape can be heat softened and then drawn through a jig. With twisted tape segments of appropriate rigidity, the segments slide in position inside the through holes and the accessible portion of the tape edge in contact with the barrel can be secured either by welding or by an adhesive compound. This assembly approach would better suit configurations (f), (g), and (i) in Fig. 1, since in configuration (h) and (j) in Fig. 1, the two more internal twisted tape segments would remain not secured and may therefore slip out of position during the lifetime of the heat sink. A two-part adhesive or a ultraviolet light cured adhesive may be used to mitigate this. The alternative assembly approach involves assembling each microchannel pipe from two half-pipes, as schematically shown by the middle (fourth) microchannel in Fig. 1(a). The twisted tape segments can be fixed to one of the half pipes along the pipe full length by welding/brazing or by an adhesive compound. Next, each half-pipe pair can be sandwiched together to form a full pipe and the seams closed by welding/brazing or by an adhesive compound.

The material selected for this numerical study, silicon, is difficult to bond. A metal alloy microchannel prototype, in copper or aluminium, may mitigate this challenge and provide an appropriate platform for performing comparative laboratory measurements of thermal and hydraulic performance, to substantiate the numerical findings of this work.

4. Conclusions

This article documented the application of conjugate heat transfer and of computational fluid dynamics to examine the effect of twisted tape inserts in a silicon microchannel heat sink, cooled by pure water at an inlet temperature of 298 K, over the Reynolds number range 100 to 500. These simulations combine individual design features of twisted tapes from past work and detail, for the first time, how these features affect the microchannel hydrothermal performance, when applied in isolation and in combination with one another. These features are: (i) radial gaps between the tape edges and the channel inner cylindrical wall, (ii) an axial twist in the tape at the three pitch distances of P = ∞, P

Fig. 20. Variation of Figure of Merit (FoM) with Reynolds number for various twisted tape designs.

= L/2 and P = L/4, (iii) segmenting the tape by one or two 90 degrees tape pitch angle steps, and (iv) alternating the direction of the helix in consecutive tape segments.

The lowest average bottom wall temperature is predicted by using a tape with no radial gap, of the finest pitch P = L/4, with two 90 degrees tape pitch angle steps, and alternating helix directions. It shows that the design features (i) to (iv) constructively combine to reduce the average bottom wall temperature by 16.13 K below that of the equivalent microchannel without any tape insert, at the same Reynolds number of 500. Using this type of design enables keeping electronic components cooler for a given electrical load. The 16.13 K lower contact temperature is significant in the context of microchip cooling that typically works at heat sink contact temperatures of around 70 degrees Celsius. Cooler microchips typically are more energy efficient and have a longer life, generating operating cost savings and a lower environmental impact. This gain comes at the cost of a heat sink higher pumping power, to overcome the friction factor that raises to a value between 2.46 and 2.74 times that of the equivalent microchannel without any tape and this cost increases with the Reynolds number. A trade-off is therefore required between the microchip full life cycle operating costs and that of its microchannel heat sink, towards which this work has provided necessary quantitative data input.

The microchannel flow analysis in this work has exposed a mechanism that is thought responsible for this temperature reduction with the alternating tape twist direction of feature (iv). This pitch reversal causes flow separation over the leading edge of the downstream helix. This separation is seen to divert cooler flow running near the axis of the microchannel towards the heated cylindrical microchannel walls. The process results in a more uniform coolant temperature.

The microchannel tape insert with no pitch reversal was predicted to achieve a microchannel wall average temperature reduction of 15.91 K at Re = 500, compared to the configuration without any tape. This appears to be still a very useful temperature reduction and avoids the complexity of assembling tape segments of alternating pitch. The flow analysis has identified to some extent the mechanism behind this performance advantage compared to having no tape insert. The tape twist displaces coolant that is running near the top wall, which is unheated, towards the bottom wall, which is heated, so that the bottom wall has a continuous supply of relatively colder coolant that displaces the coolant being heated on it. Using a finer pitch of P = L/4 enhances this effect compared to the coarser pitch of P = L/2.

Closing any radial gap between the tape and the microchannel cylindrical wall is shown by the numerical simulations to be advantageous both to the thermal performance and to the hydraulic performance of the heat sink. This dual advantage comes from the thermal conduction through the contact between these two surfaces and from the elimination of tape tip gap leakage hydraulic losses.

Inserting a straight tape in the microchannel heat sink delivers a lower temperature than with no tape. This simple arrangement may have manufacturing advantages over the more complex geometries presented herein, but this paper has shown by numerical modelling some performance gains from adding tape twist and 90 degrees angle steps that may meet the lower temperature requirement of future generation microchips.

From a methodological prospective, the Figure of Merit (FoM) used in this paper was found to be a useful performance quality indicator, as it presents the trade-off between any heat removal gain and frictional loss penalty from implementing the tape inserts as a single, computable quantity. It appears to be a good candidate performance function for computer-assisted optimization processes such as techniques based on artificial intelligence. The conjugate heat transfer analysis and flow simulation has shown to be able to provide sound physical arguments to explain the predicted performance of the different tape inserts, thereby providing robust foundations and a sound physical base for the design and optimization process of microchannel heat sinks.

There are a few manufacturing options for the physical prototyping and industrialization of the microchannel heat sinks. Their merits and challenges were explored. They build confidence in the ability of progressing to a physical prototype that can be used to laboratory test the hydro-mechanical performance of the twisted tape microchannel heat sinks.

CRediT authorship contribution statement

Abdullah Masoud Ali: Conceptualization, Data curation, Formal analysis, Methodology, Software, Validation, Visualization, Writing – original draft. **Aldo Rona:** Formal analysis, Funding acquisition, Methodology, Project administration, Supervision, Writing – original draft, Writing – review & editing. **Matteo Angelino:** Formal analysis, Methodology, Supervision, Writing – review & editing.

Declaration of Competing Interest

The authors declare that they have no known competing financial interests or personal relationships that could have appeared to influence the work reported in this paper.

Acknowledgements

References

Abolarin, S.M., Everts, M., Meyer, J.P., 2019. Heat transfer and pressure drop characteristics of alternating clockwise and counter clockwise twisted tape inserts in the transitional flow regime. Int. J. Heat Mass Transf. 133, 203–217.

Adham, A.M., Mohd-Ghazali, N., Ahmad, R., 2012. Optimization of an ammonia-cooled rectangular microchannel heat sink using multi-objective non-dominated sorting genetic algorithm (NSGA2). Heat Mass Transf. 48 (10), 1723–1733.

Adham, M.A., Mohd-Ghazali, N., Ahmad, R., 2013. Thermal and hydrodynamic analysis of microchannel heat sinks: a review. Renew. Sustain. Energy Rev. 21, 614–622.

Alam, T., Kim, M.-H., 2018. A comprehensive review on single phase heat transfer enhancement techniques in heat exchanger applications. Renew. Sustain. Energy Rev. 81, 813–839.

Alfaryjat, A., Miron, L., Pop, H., Apostol, V., Stefanescu, M.-F., Dobrovicescu, A., 2019. Experimental investigation of thermal and pressure performance in computer cooling systems using different types of nanofluids. Nanomaterials (Basel) 9 (9), 1231.

Ali, A.M., Rona, A., Kadhim, H.T., Angelino, M., Gao, S., 2021. Thermo-hydraulic performance of a circular microchannel heat sink using swirl flow and nanofluid. Appl. Therm. Eng. 191, 116817.

Ali, A.M., Angelino, M., Rona, A., 2021. Numerical analysis on the thermal performance of microchannel heat sinks with Al_2O_3 nanofluid and various fins. Appl. Therm. Eng. 198, 117458.

Ali, A.M., Angelino, M., Rona, A., 2022. Physically consistent implementation of the mixture model for modelling nanofluid conjugate heat transfer in minichannel heat sinks. Appl. Sci. 12 (14), 7011.

Awais, M., Bhuiyan, A.A., 2018. Heat transfer enhancement using different types of vortex generators (VGs): a review on experimental and numerical activities. Therm. Sci. Eng. Progress 5, 524–545.

Bahiraei, M., Heshmatian, S., 2017. Efficacy of a novel liquid block working with a nanofluid containing graphene nanoplatelets decorated with silver nanoparticles compared with conventional CPU coolers. Appl. Therm. Eng. 127, 1233–1245.

Bahiraei, M., Mazaheri, N., Hassanzamani, S.M., 2019. Efficacy of a new graphene–platinum nanofluid in tubes fitted with single and twin twisted tapes regarding counter and co-swirling flows for efficient use of energy. Int. J. Mech. Sci. 150, 290–303.

Bahiraei, M., Jamshidmofid, M., Goodarzi, M., 2019. Efficacy of a hybrid nanofluid in a new microchannel heat sink equipped with both secondary channels and ribs. J. Mol. Liq. 273, 88–98.

Barba, A., Musi, B., Spiga, M., 2006. Performance of a polymeric heat sink with circular microchannels. Appl. Therm. Eng. 26 (8), 787–794.

Bazidi-Tehrani, F., Khanmohamadi, S.M., Vasefi, S.I., 2020. Evaluation of turbulent forced convection of non-Newtonian aqueous solution of CMC/CuO nanofluid in a tube with twisted tape inserts. Adv. Powder Technol. 31 (3), 1100–1113.

Bhandari, P., Prajapati, Y.K., 2021. Thermal performance of open microchannel heat sink with variable pin fin height. Int. J. Therm. Sci. 159, 106609.

Bhuiya, M.M.K., Chowdhury, M.S.U., Saha, M., Islam, M.T., 2013. Heat transfer and friction factor characteristics in turbulent flow through a tube fitted with perforated twisted tape inserts. Int. Commun. Heat Mass Transfer 46, 49–57.

Cengel, Y.A. 2010. *Fluid Mechanics.* Tata McGraw-Hill Education.

Chai, L., Wang, L., Bai, X., 2018. Thermohydraulic performance of microchannel heat sinks with triangular ribs on sidewalls – Part 1: local fluid flow and heat transfer characteristics. Int. J. Heat Mass Transf. 127, 1124–1137.

Chai, L., Wang, L., Bai, X., 2019. Thermohydraulic performance of microchannel heat sinks with triangular ribs on sidewalls – Part 2: average fluid flow and heat transfer characteristics. Int. J. Heat Mass Transf. 128, 634–648.

Chen, Y., Cheng, P., 2005. An experimental investigation on the thermal efficiency of fractal tree-like microchannel nets. Int. Commun. Heat Mass Transfer 32 (7), 931–938.

Cheng, Y., 2007. Numerical simulation of stacked microchannel heat sink with mixing-enhanced passive structure. Int. Commun. Heat Mass Transfer 34 (3), 295–303.

Choquette, S.F., Faghri, M., Charmchi, M., Asako, Y. 1996. *Optimum design of microchannel heat sinks.* American Society of Mechanical Engineers, Dynamic Systems Control Division DSC, **59**: p. 115.

Deng, D., Zeng, L., Sun, W., 2021. A review on flow boiling enhancement and fabrication of enhanced microchannels of microchannel heat sinks. Int. J. Heat Mass Transf. 175, 121332.

Eiamsa-ard, S., 2010. Study on thermal and fluid flow characteristics in turbulent channel flows with multiple twisted tape vortex generators. Int. Commun. Heat Mass Transfer 37 (6), 644–651.

Eiamsa-ard, S., Promvonge, P., 2010. Performance assessment in a heat exchanger tube with alternate clockwise and counter-clockwise twisted-tape inserts. Int. J. Heat Mass Transf. 53 (7), 1364–1372.

Eiamsa-ard, S., Thianpong, C., Eiamsa-ard, P., Promvonge, P., 2010. Thermal characteristics in a heat exchanger tube fitted with dual twisted tape elements in tandem. Int. Commun. Heat Mass Transfer 37 (1), 39–46.

Eiamsa-Ard, S., Nanan, K., Wongcharee, K., Yongsiri, K., Thianpong, C., 2015. Thermohydraulic performance of heat exchanger tube equipped with single-, double-, and triple-helical twisted tapes. Chem. Eng. Commun. 202 (5), 606–615.

Gamrat, G., Favre-Marinet, M., Asendrych, D., 2005. Conduction and entrance effects on laminar liquid flow and heat transfer in rectangular microchannels. Int. J. Heat Mass Transf. 48 (14), 2943–2954.

Ghani, I.A., Sidik, N.A.C., Mamat, R., Najafi, G., Ken, T.L., Asako, Y., Japar, W.M.A.A., 2017. Heat transfer enhancement in microchannel heat sink using hybrid technique of ribs and secondary channels. Int. J. Heat Mass Transf. 114, 640–655.

Ghasemi, S.E., Ranjbar, A., Hosseini, M., 2017. Numerical study on effect of CuO-water nanofluid on cooling performance of two different cross-sectional heat sinks. Adv. Powder Technol. 28 (6), 1495–1504.

Guo, J., Fan, A., Zhang, X., Liu, W., 2011. A numerical study on heat transfer and friction factor characteristics of laminar flow in a circular tube fitted with center-cleared twisted tape. Int. J. Therm. Sci. 50 (7), 1263–1270.

Harley, J.C., Huang, Y., Bau, H.H., Zemel, J.N., 1995. Gas flow in micro-channels. J. Fluid Mech. 284, 257–274.

He, Y., Liu, L., Li, P., Ma, L., 2018. Experimental study on heat transfer enhancement characteristics of tube with cross hollow twisted tape inserts. Appl. Therm. Eng. 131, 743–749.

Hung, T.-C., Yan, W.-M., 2012. Effects of tapered-channel design on thermal performance of microchannel heat sink. Int. Commun. Heat Mass Transfer 39 (9), 1342–1347.

Hunt, J.C., Wray, A.A., Moin, P., 1988. *Eddies, streams, and convergence zones in turbulent flows.* In: *Studying Turbulence using Numerical Databases, 2.* Proceedings of the Summer Program 1988. Center for Turbulence Research, Stanford, pp. 193–208.

Jang, S.P., Choi, S.U.S., 2006. Cooling performance of a microchannel heat sink with nanofluids. Appl. Therm. Eng. 26 (17), 2457–2463.

Jing, D., He, L., 2019. Numerical studies on the hydraulic and thermal performances of microchannels with different cross-sectional shapes. Int. J. Heat Mass Transf. 143, 118604.

Jing, D., Song, J., Sui, Y., 2020. Hydraulic and thermal performances of laminar flow in fractal treelike branching microchannel network with wall velocity slip. Fractals 28 (2), 2050022.

Kandlikar, S.G., Bapat, A.V., 2007. Evaluation of jet impingement, spray and microchannel chip cooling options for high heat flux removal. Heat Transfer Eng. 28 (11), 911–923.

Kandlikar, S.G., Grande, W.J., 2003. Evolution of microchannel flow passages-thermohydraulic performance and fabrication technology. Heat Transfer Eng. 24 (1), 3–17.

Khoshvaght-Aliabadi, M., Feizabadi, A., 2020. Performance intensification of tubular heat exchangers using compound twisted-tape and twisted-tube. Chem. Eng. Process. - Process Intensification 148, 107799.

Kleiner, M.B., Kuhn, S.A., Haberger, K., 1995. High performance forced air cooling scheme employing microchannel heat exchangers. IEEE Trans. Compon. Packag. Manuf. Technol. Part A: 18 (4), 795–804.

Koşar, A., 2010. Effect of substrate thickness and material on heat transfer in microchannel heat sinks. Int. J. Therm. Sci. 49 (4), 635–642.

Li, P., Guo, D., Huang, X., 2020. Heat transfer enhancement, entropy generation and temperature uniformity analyses of shark-skin bionic modified microchannel heat sink. Int. J. Heat Mass Transf. 146, 118846.

Liu, X., Li, C., Cao, X., Yan, C., Ding, M., 2018. Numerical analysis on enhanced performance of new coaxial cross twisted tapes for laminar convective heat transfer. Int. J. Heat Mass Transf. 121, 1125–1136.

Lu, G., Zhai, X., 2019. Analysis on heat transfer and pressure drop of a microchannel heat sink with dimples and vortex generators. Int. J. Therm. Sci. 145, 105986.

Manglik, R.M., Bergles, A.E. 2003. *Swirl flow heat transfer and pressure drop with twisted-tape inserts*, in *Advances in Heat Transfer*, J.P. Hartnett, et al., Editors. Elsevier. p. 183-266.

Mohammed, H.A., Gunnasegaran, P., Shuaib, N.H., 2011. Numerical simulation of heat transfer enhancement in wavy microchannel heat sink. Int. Commun. Heat Mass Transfer 38 (1), 63–68.

Mohammed, H.A., Gunnasegaran, P., Shuaib, N.H., 2011. Influence of various base nanofluids and substrate materials on heat transfer in trapezoidal microchannel heat sinks. Int. Commun. Heat Mass Transfer 38 (2), 194–201.

Mondal, M., Misra, R.P., De, S., 2014. Combined electroosmotic and pressure driven flow in a microchannel at high zeta potential and overlapping electrical double layer. Int. J. Therm. Sci. 86, 48–59.

Narendran, G., Gnanasekaran, N., Perumal, D.A., 2020. Thermodynamic irreversibility and conjugate effects of integrated microchannel cooling device using TiO_2 nanofluid. Heat Mass Transf. 56 (2), 489–505.

Peng, X.F., Peterson, G.P., Wang, B.X., 1994. Heat transfer characteristics of water flowing through microchannels. Exp. Heat Transfer 7 (4), 265–283.

Ponnada, S., Subrahmanyam, T., Naidu, S.V., 2019. A comparative study on the thermal performance of water in a circular tube with twisted tapes, perforated twisted tapes and perforated twisted tapes with alternate axis. Int. J. Therm. Sci. 136, 530–538.

Radenac, E., Gressier, J., Millan, P., 2014. Methodology of numerical coupling for transient conjugate heat transfer. Comput. Fluids 100, 95–107.

Roache, P.J., 1998. Verification and validation in computational science and engineering, Vol. 895. Hermosa Albuquerque, NM.

Schwer L.E. 2008. *Is your mesh refined enough? Estimating discretization error using GCI.* 7th LS-DYNA Anwenderforum, **1**(1), 45-54.

Singh, V., Chamoli, S., Kumar, M., Kumar, A., 2016. Heat transfer and fluid flow characteristics of heat exchanger tube with multiple twisted tapes and solid rings inserts. Chem. Eng. Process. Process Intensif. 102, 156–168.

Tunc, G., Bayazitoglu, Y., 2002. Heat transfer in rectangular microchannels. Int. J. Heat Mass Transf. 45 (4), 765–773.

Tusar, M., Ahmed, K., Bhuiya, M., Bhowmik, P., Rasul, M., Ashwath, N., 2019. CFD study of heat transfer enhancement and fluid flow characteristics of laminar flow through tube with helical screw tape insert. Energy Procedia 160, 699–706.

Varun, Garg, M.O., Nautiyal, H., Khurana, S., Shukla, M.K., 2016. Heat transfer augmentation using twisted tape inserts: a review. Renew. Sustain. Energy Rev. 63, 193–225.

Wang, H., Chen, Z., Gao, J., 2016. Influence of geometric parameters on flow and heat transfer performance of micro-channel heat sinks. Appl. Therm. Eng. 107, 870–879.

Wang, Z.-H., Wang, X.-D., Yan, W.-M., Duan, Y.-Y., Lee, D.-J., Xu, J.-L., 2011. Multi-parameters optimization for microchannel heat sink using inverse problem method. Int. J. Heat Mass Transf. 54 (13), 2811–2819.

Waqas, H., Khan, S.A., Farooq, U., Muhammad, T., Alshehri, A., Yasmin, S., 2022. Thermal transport analysis of six circular microchannel heat sink using nanofluid. Sci. Rep. 12 (1), 8035.

Webb, R.L., Kim, N.J., 2005. *Principles of enhanced heat transfer*, second ed. Taylor & Francis, New York.

Wu, J.M., Tao, W.Q., 2008. Numerical study on laminar convection heat transfer in a rectangular channel with longitudinal vortex generator. Part A: verification of field synergy principle. Int. J. Heat Mass Transf. 51 (5), 1179–1191.

Zheng, W., Sun, J., Ma, C., Yu, Q., Zhang, Y., Niu, T., 2021. Numerical study of fluid flow and heat transfer characteristics in a cone-column combined heat sink. Energies 14 (6), 1605.

Zhimin, W., Fah, C.K. 1997. *The optimum thermal design of microchannel heat sinks*. in *Proceedings of the 1997 1st Electronic Packaging Technology Conference (Cat. No.97TH8307)*.

Zhuan, R., Wang, W., 2013. Boiling heat transfer characteristics in a microchannel array heat sink with low mass flow rate. Appl. Therm. Eng. 51 (1), 65–74.